

7 ABSTRACT: Submesoscale currents, comprising fronts and mixed-layer eddies, exhibit a dual
8 cascade of kinetic energy: a forward cascade to dissipation scales at fronts and an inverse cascade
9 from mixed-layer eddies to mesoscale eddies. Within a coarse-graining framework using both
10 spatial and temporal filters, we show that this dual cascade can be captured in simple mathematical
11 form obtained by writing the cross-scale energy flux in the local principal strain coordinate system,
12 wherein the flux reduces to the the sum of two terms, one proportional to the convergence and the
13 other proportional to the strain. The strain term is found to cause the inverse energy flux to larger
14 scales while an approximate equipartition of the convergent and strain terms capture the forward
15 energy flux, demonstrated through model-based analysis and asymptotic theory. A consequence
16 of this equipartition is that the frontal forward energy flux is simply proportional to the frontal
17 convergence. In a recent study, it was shown that the Lagrangian rate of change of quantities
18 like the divergence, vorticity and horizontal buoyancy gradient are proportional to convergence at
19 fronts implying that horizontal convergence drives frontogenesis. We show that these two results
20 imply that the primary mechanism for the forward energy flux at fronts is frontogenesis. We
21 also analyze the energy flux through a Helmholtz decomposition and show that the rotational
22 components are primarily responsible for the inverse cascade while a mix of the divergent and
23 rotational components cause the forward cascade, consistent with our asymptotic analysis based
24 on the principal strain framework.

25 **1. Introduction**

26 Most of the kinetic energy (KE) in the earth's oceans is found in mesoscale eddies consequent
27 of which, understanding the mechanisms and pathways of their generation and dissipation is of
28 fundamental importance (Ferrari and Wunsch 2009). Since they are approximately in geostrophic
29 balance, classical geostrophic turbulence theory (Salmon 1998) provides a paradigm wherein
30 available potential energy (APE) created by the action of large scale wind stress and surface
31 buoyancy fluxes is converted into kinetic energy through baroclinic instability. Nonlinear eddy-
32 eddy interactions then induce an inverse cascade of this kinetic energy to larger eddy scales, with
33 their dissipation primarily limited to occur at the boundaries, both at the ocean bottom and, as has
34 been demonstrated recently, the air-sea interface (Ma et al. 2016; Renault et al. 2016, 2018, 2019;
35 Rai et al. 2021). Studies over the past two decades have, however, found that mesoscale eddies
36 can have significant energy exchanges with smaller and faster oceanic components comprising
37 submesoscale mixed layer eddies (MLEs) and fronts (Thomas et al. 2008; McWilliams 2016), and
38 inertia gravity waves (IGWs) (Thomas 2012; Xie and Vanneste 2015; Taylor and Straub 2016;
39 Alford et al. 2016; Jing et al. 2017; Barkan et al. 2017; Rocha et al. 2018; Thomas and Daniel 2021;
40 Barkan et al. 2021). Mesoscale eddies have horizontal length scales in the range $O(10\text{km}-100\text{km})$
41 and time scales of weeks to a months. MLEs typically have $O(1-10\text{km})$ while cross-frontal scales
42 can be as small as tens of metres. While MLEs can last a few days, frontal time scales can overlap
43 with those of IGWs that are physically constrained to be faster than the local Coriolis frequency.

44 Like mesoscale eddies, MLEs are also formed through baroclinic instability but of the near-
45 surface mixed layer (Boccaletti et al. 2007), which is deeper during the winter season due to surface
46 cooling driven convective mixing (Mensa et al. 2013; Brannigan et al. 2015; Callies et al. 2015;
47 Thompson et al. 2016). In fact layered quasi-geostrophic models that have been a long standing
48 framework for studying mesoscale eddies also reproduce MLEs with a shallow upper layer, but not
49 fronts (Callies et al. 2016). Fronts, which are highly anisotropic structures, are formed through a
50 multitude of mechanisms (Hoskins and Bretherton 1972; McWilliams 2017; Srinivasan et al. 2017)
51 that involve the background gradients provided by both mesoscale eddies and MLEs, but also the
52 turbulence in the mixed layer (McWilliams et al. 2015; Wenegrat and McPhaden 2016; McWilliams
53 2017). Energetically, the generation of both fronts and MLEs involves a conversion of mixed layer
54 APE to KE, but unlike MLEs, fronts also have a significant ageostrophic flow component in the

55 cross-front direction i.e. the ageostrophic secondary circulation (ASC). Frontal ASCs are highly
56 asymmetric, with strong downwelling and weak upwelling, and this manifests as a large visible
57 negative value of the divergence in the mixed layer, $\delta = u_x + v_y$ (u and v are the velocities along the
58 zonal, x , and meridional, y , directions). Heuristically one might expect that the similarity in the
59 generation and balance of mesoscale eddies and MLEs might lead to similar nonlinear dynamics.
60 A recent study by Schubert et al. (2020) employed a coarse graining approach (Aluie et al. 2018)
61 to explicitly demonstrate that MLEs undergo an inverse energy cascade to mesoscales, echoing the
62 inverse energy transfer of mesoscale eddies themselves to larger scales. In particular they were able
63 to provide a visual and dynamical demonstration of the absorption of MLEs into mesoscale eddies.
64 They also show that the energy transfer at smaller scales occurs primarily at frontal features and is
65 forward i.e. from large to small scales. This is consistent with previous studies that suggest that
66 ageostrophic motions might be responsible for forward energy cascades found at submesoscales
67 (Capet et al. 2008b).

68 In this study we examine the cross scale flux of kinetic energy in realistic submesoscale resolving
69 numerical simulations of the North Atlantic. Instead of the traditionally used spectral energy flux
70 approach (Scott and Wang 2005; Scott and Arbic 2007; Klein et al. 2008; Capet et al. 2008b,a;
71 Molemaker et al. 2010; Barkan et al. 2015; Wang et al. 2019; Klein et al. 2019; Ajayi et al. 2021;
72 Siegelman et al. 2022), we employ the filter-based coarse graining framework to compute energy
73 fluxes across both spatial (Aluie et al. 2018; Srinivasan et al. 2019; Schubert et al. 2020) and
74 temporal (Barkan et al. 2017, 2021; Garabato et al. 2022; Zhang et al. 2021b,a) scales. Figure 1
75 shows the spatial structure of the spatial KE flux from our 500 m horizontal resolution run (details
76 in Section 2) for a filter-scale of 4km (Π_h^4 , representing the horizontal KE transfer from scales
77 larger than 4km to those smaller) during the month of January. Echoing the results of Schubert
78 et al. (2020), we find that the flux is largest at the frontal features which can be identified as regions
79 of strong convergence ($-\delta$) and buoyancy gradient, $|\nabla b|$. Furthermore, while some of the regions
80 of strong forward transfer are clearly at fronts that lie on the edges of large mesoscale anticyclones
81 (leading to the possibility that these are generated through strain-induced frontogenesis) most other
82 regions are at fronts associated with smaller scale eddies or sometimes none at all. This indicates
83 that the mechanism of energy flux at fronts is agnostic to the mechanism of frontal generation.
84 The choice of 4km filter-scale in Fig. 1 is not specific and represents a typical length scale in the

85 submesoscale range (in Sec 4a we show that this actually corresponds to an equivalent spectral
 86 length scale of $\lambda_{sp} = 9.6$ km). In the rest of the paper, we employ a wide range of filter-scales for
 87 analysis starting from the grid scale till beyond mesoscale eddy length scales.

101 To make the association between fronts and the energy flux stronger and foreshadow the results
 102 in our paper ahead, we compare the energy flux across the 4 km scale (Π_h^4) averaged over the flow
 103 domain seen in Fig. 1 with that conditionally averaged on fronts only (given by the region satisfying
 104 $\nabla b > 1.5 \times 10^{-7} \text{s}^{-2}$) as a function of depth (Fig. 2a). We note that both the frontal-averaged flux (red
 105 curve) and the domain-averaged flux (blue curve) are positive over this depth, i.e. a positive energy
 106 flux from scales larger than 4km to smaller or equivalently a *forward* flux. The front-averaged
 107 forward flux is also two orders of magnitude larger, supporting the visual inference from Fig. 1 that
 108 the energy flux at this scale is predominantly at fronts. The vertical structure of the front-averaged
 109 flux closely resembles that of the front-averaged convergence, $-\bar{\delta}_{fronts}^4$ (where $\bar{\delta}^4$ is the divergence
 110 smoothed at the same 4 km scale for consistency) and the kinetic energy at scales smaller than 4
 111 km, \mathcal{E}^4 , averaged at fronts, \mathcal{E}'^4_{fronts} . It should be noted that the rate of change of \mathcal{E}^4 due to the
 112 energy exchange with larger scales is precisely, Π_h^4 , i.e.

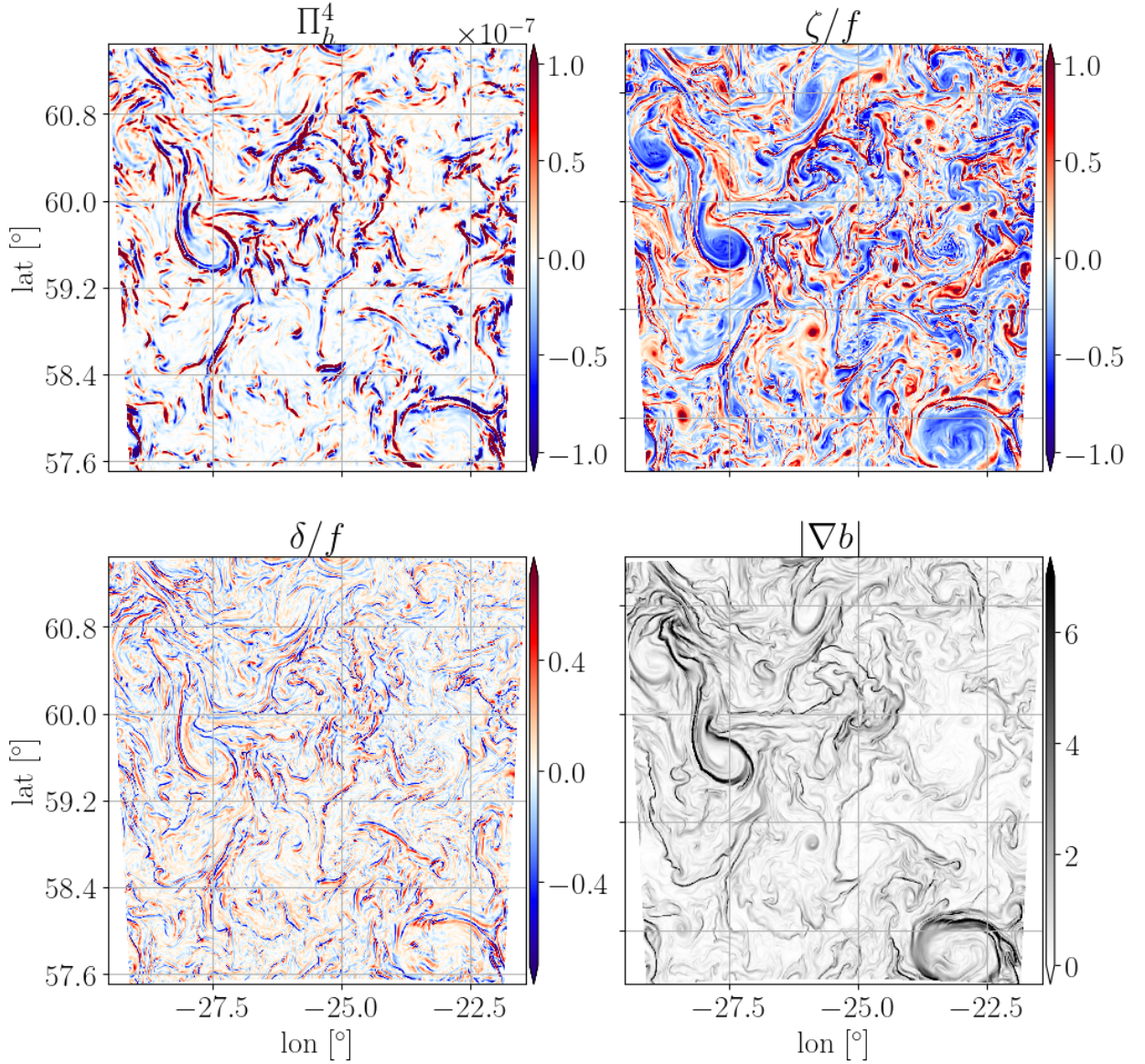
$$\left(\frac{D\mathcal{E}^4}{Dt} \right)_{transfer} = \Pi_h^4. \quad (1)$$

113 By plotting the $\Pi_{h,fronts}^4$ against $-\bar{\delta}_{fronts}^4 \mathcal{E}'^4_{fronts}$ (a natural choice, given that the two quantities
 114 have identical dimensions) we find the simple result that the relationship is *linear*, so that $\Pi_h^4 \propto$
 115 $-\bar{\delta}_{fronts}^4 \mathcal{E}'^4_{fronts}$. But from (1) we get

$$\frac{1}{\mathcal{E}'^4_{fronts}} \left(\frac{D\mathcal{E}^4}{Dt} \right)_{transfer,fronts} \propto -\bar{\delta}_{fronts}^4. \quad (2)$$

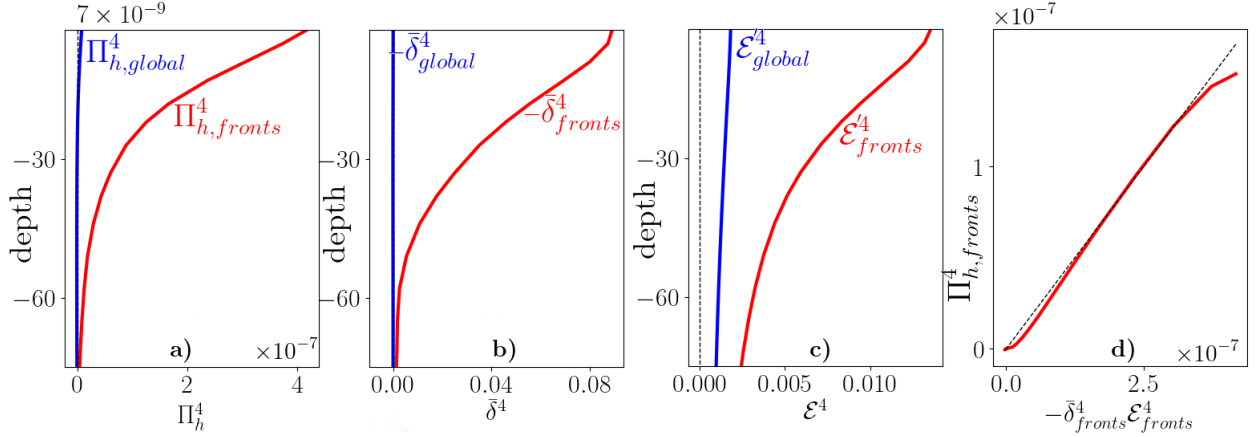
116 The results above can be summarized as follows: the rate of change of kinetic energy (the energy
 117 flux) at around 4km scales during the winter season in this region is predominantly at fronts while
 118 the *relative* rate of change of frontal kinetic energy is simply governed by the convergence as give
 119 by (2).

120 The entire analysis above was based on a combination of dimensional considerations and simple
 121 model-based heuristics, but is a key result of this study. We show that (2) can in fact be derived from



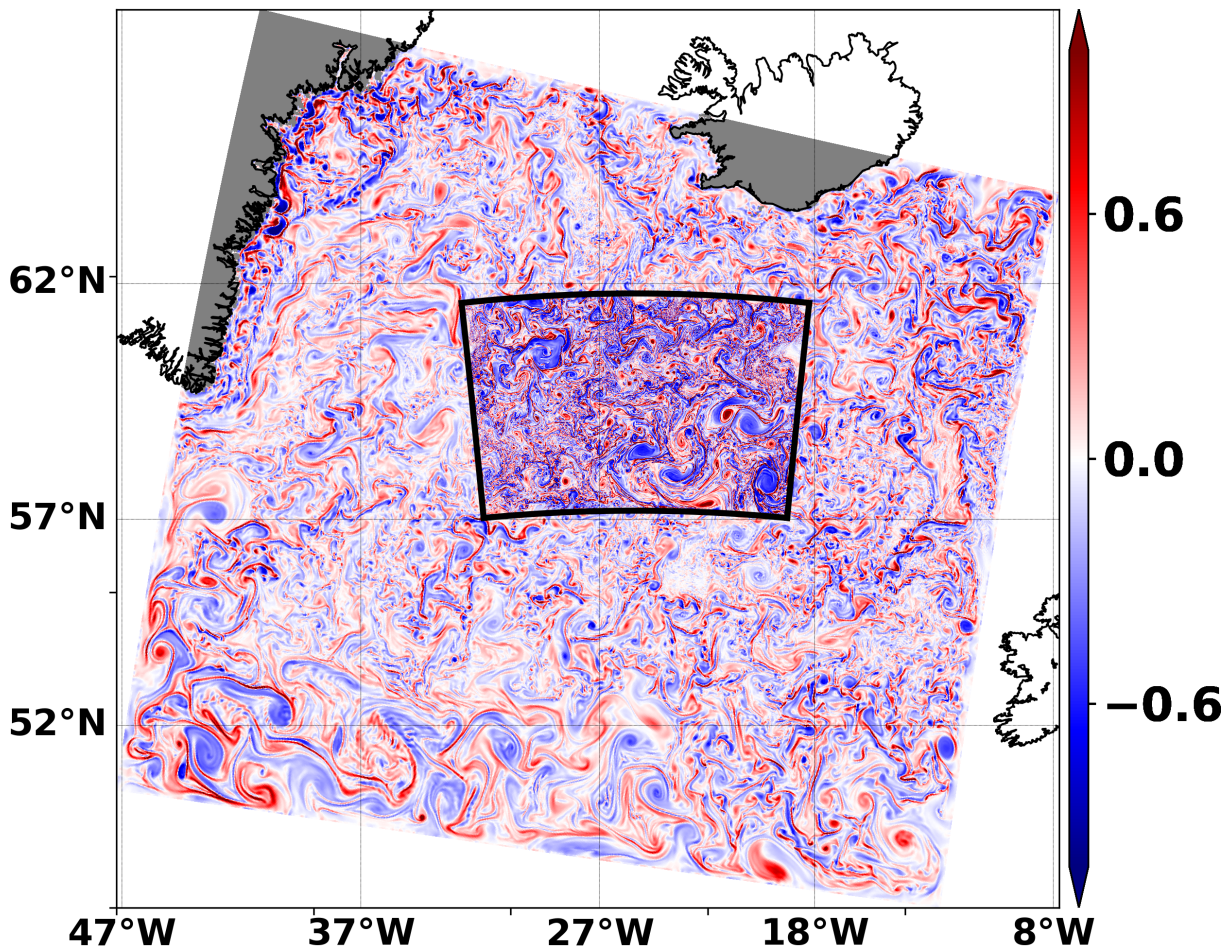
88 FIG. 1. A snapshot of horizontal cross-scale energy flux Π_h^4 [m^2s^{-3}] on January 7th (i.e. the winter season),
 89 where the superscript indicates a filterscale of 4 km, the energy transferred from scales larger than 4 km to finer
 90 scales at a ocean surface [Note that this is equivalent to an effective spectral scale, $\lambda_{sp} = 9.6$ km (see Section
 91 4a)]. Also shown are the surface vorticity [s^{-1}], $\zeta = v_x - u_y$ and the divergence [s^{-1}], $\delta = u_x + v_y$ normalized
 92 with the Coriolis paramter, f and the magnitude of the horizontal buoyancy gradient, $|\nabla b|$ [s^{-2}]. The horizontal
 93 model resolution here is 500 m.

122 first principles by writing the energy flux in principal strain coordinates (Section 3) followed by a
 123 combination of detailed model-based analysis (Section 4, including an analysis of the energy flux



94 FIG. 2. Plots, as a function of depth [m], of (a) Π_h^4 [m^2s^{-3}], the horizontal energy flux from scales larger
 95 than 4km to smaller scales, (b) $-\bar{\delta}^4$ [s^{-1}], the convergence smoothed at a 4km scale and, (c) \mathcal{E}^4 [m^2s^{-2}], the
 96 kinetic energy of scales finer than 4 km, either spatially averaged over the entire flow domain shown in Fig. 1
 97 (marked by the subscript, ‘global’ and in blue) or spatially averaged only on fronts defined by the region having
 98 $|\nabla b| > 1.5 \times 10^{-7} \text{s}^{-2}$ (marked by the subscript, ‘fronts’ and in red); temporal averaging is also performed over the
 99 winter months of January, February and March on top of the indicated spatial averaging. (d) A plot of $\Pi_{h,fronts}^4$
 100 in a) versus $-\bar{\delta}_{fronts}^4 \mathcal{E}_{fronts}^4$ [the product of b) and c)].

124 using the Helmholtz decomposition in Section 4c) and asymptotic theory (Section 5). Section 5
 125 connects the results here with the theory of frontogenesis proposed by Barkan et al. (2019)
 126 demonstrating that convergence drives frontogenesis, a result that we show here also applies to the
 127 cross-scale energy flux through the form of (2). In this paper we do not explore the seasonality
 128 of the forward and inverse energy cascades as has been suggested in recent work (Garabato et al.
 129 2022) that analyses temporal energy transfers from observational data (in particular the OSMOSIS
 130 current meter array) and find an inverse energy cascade in winter from submesoscales to mesoscales
 131 but a forward energy transfer in late spring. We instead limit our attention to the winter season in
 132 the North Atlantic when the submesoscales are strongest and examine the cross-scale KE fluxes and
 133 their structure at submesoscale spatial and temporal scales. We also briefly discuss a potentially
 134 alternative pathway for forward energy cascade, namely symmetric instability accompanied by
 135 some analysis and discussions involving the vertical component of the energy flux, Π_v^ℓ , and the
 136 corresponding geostrophic shear production, Π_{vg}^ℓ (Section 6b). In concurrent (Barkan et al. 2021)
 137 and upcoming studies we also examine the energy exchanges between eddies, fronts and IGWs.



139 FIG. 3. A snapshot of the normalized surface vorticity, ζ/f , on February 8, obtained from the 2 km (outer
 140 nest) and 500 m (inner nest) horizontal resolution nested ROMS simulations. The 2km run, forced by a 6 km
 141 resolution North Atlantic run (not shown here), spans the North Atlantic region between Greenland and Iceland.
 142 The actual analysis region (shown in Fig. 1) for the 2 km and 500 m runs in this work is a square region spanning
 143 about two-thirds of the inner 500 m nest here.

144 Numerical solutions are conducted using the Regional Ocean Modeling System (ROMS) a
 145 split-explicit hydrostatic primitive model (Shchepetkin and McWilliams 2005). A nested grid
 146 hierarchy with one-way nesting is employed; a 6km resolution parent grid run forced on its external
 147 boundaries by climatology is run beginning 1 January, 1999 for two years with only the third
 148 year run used to force a 2 km run at the boundaries; the 2 km run is then subsequently used to

149 force and run a submesoscale-permitting 500 m resolution run. A surface vorticity snapshot in
150 early February is plotted in Fig. 3 highlighting the 2 km-500 m nested hierarchy and the stronger
151 submesoscale field of the 500 m resolution model. The actual analysis domain employed in this
152 work is an approximately 430 km \times 430 km region within the 500 m nested grid, displayed in
153 Fig. 1. The air-sea interface is forced with the Climate Forecast System Reanalysis (CFSR)(Saha
154 et al. 2014; Dee et al. 2014) atmospheric product low pass filtered using a one-day filter to eliminate
155 high frequency forcing that would generate Near-inertial internal waves (NIWs). We only use the
156 winter months (January, February and March 2001) of the 500 m and 2 km runs for analysis in this
157 study since these are the months when submesoscale MLEs and fronts are especially active. The
158 solutions used for analysis in this paper have been validated extensively in our concurrent study
159 (Barkan et al. 2021) against satellite altimetry and current meter observations in the region so we
160 refer the readers to that paper.

161 **3. Dynamics in principal strain coordinates**

162 We compute the energy flux across scales using the so-called coarse graining approach which
163 entails a method for decomposing the flow field into small and large scales for spatial transfers
164 (Eyink and Aluie 2009; Aluie et al. 2018), and fast and slow scales for temporal transfers (Barkan
165 et al. 2017). These are accomplished using a simple low-pass filtering (or smoothing) operator.
166 In this study we separately compute cross-scale transfers across spatial and temporal scales rather
167 than a joint spatio-temporal approach. While previous studies have been limited to computing
168 either spatial (Aluie et al. 2018; Schubert et al. 2020) or temporal scale-to-scale transfers (Barkan
169 et al. 2017, 2021), we compute both to demonstrate the robustness of our analysis framework.
170 Furthermore, in the absence of IGWs (which is true for the simulations employed here) slower
171 (faster) scales correspond to larger (smaller) ones and this should be reflected in the cross-scale
172 energy fluxes.

173 *a. Scale-to-scale energy flux*

174 We decompose the velocity fields into scales smaller (faster) and larger (slower) than a given
175 length scale ℓ (time scale τ) with a low-pass filtering function; this is chosen to be a uniform
176 filter (also referred to as a boxcar or tophat filter) for the spatial filtering (Aluie et al. 2018)

177 and a Butterworth filter for the temporal (Barkan et al. 2021). The uniform filter is sharp in
 178 physical space but the Butterworth is spectrally sharp. These filter choices and their implications
 179 are discussed in Section 4a (in particular, see the discussion around Fig. 6.). Since the theory
 180 applies to both spatial and temporal filters, we identify the slower (larger) component as \bar{u}_i and
 181 the faster (smaller) component as u'_i where $i \in [1, 2]$ and $(u_1, u_2) \equiv (u, v)$. In other words, because
 182 $u_i = \bar{u}^\ell + u'^\ell = \bar{u}^\tau + u'^\tau \equiv \bar{u} + u'$, we derive our expressions in general and for presentation of our
 183 results, we use τ (units in hours) superscript for the temporal transfers and ℓ (units in km) for the
 184 spatial. We call the \bar{u} and u' fields as coarse and fine fields respectively. The energy transfer from
 185 scales finer than a certain scale to coarser scales is then (Aluie et al. 2018)

$$\begin{aligned} \Pi = & - \underbrace{(\tau_{uu}\bar{u}_x + \tau_{uu}(\bar{u}_y + \bar{v}_x) + \tau_{uu}\bar{v}_x)}_{\Pi_h} \\ & - \underbrace{(\tau_{uv}\bar{u}_z + \tau_{vw}\bar{v}_z)}_{\Pi_v}. \end{aligned} \quad (3)$$

186 where Π_h and Π_v are the vertical and horizontal energy flux terms. The Leonard's stress term
 187 (Leonard 1975) is $\tau_{uv} = \overline{u'v} - \bar{u}'\bar{v}'$, and similarly for the other terms. Since for filters, $\bar{u}', \bar{v}' \neq 0$ (i.e.
 188 the filter operator is not a Reynolds' operator), $\tau_{uv} \neq \overline{u'v'}$. The horizontal component can be further
 189 expressed in the form,

$$\Pi_h = -\boldsymbol{\tau} : \bar{\boldsymbol{S}} = - \begin{bmatrix} \tau_{uu} & \tau_{uv} \\ \tau_{uv} & \tau_{vv} \end{bmatrix} \begin{bmatrix} \bar{u}_x & (\bar{u}_y + \bar{v}_x)/2 \\ (\bar{u}_y + \bar{v}_x)/2 & \bar{v}_y, \end{bmatrix} \quad (4)$$

190 where the $:$ operator represents a tensor dot product operation (a term-by-term product followed
 191 by summation). The expression in (4) can be identified as “the stress of the finer scales times the
 192 strain of the coarser scale”.

193 We rotate our (x, y) coordinate axis along the vertical by angle $\theta(x, y)$ at every point in space,
 194 such that in the new local coordinate system, the strain tensor, \bar{S}_{ij} , is diagonal. Such a $\theta(x, y)$
 195 always exists because \bar{S}_{ij} is a symmetric tensor. It is straightforward to show that that the precise

196 form this diagonal tensor takes is

$$[\bar{S}] = \begin{bmatrix} (\bar{\delta} + \bar{\alpha})/2 & 0 \\ 0 & (\bar{\delta} - \bar{\alpha})/2 \end{bmatrix} \quad (5)$$

197 Where the coarse-scale divergence, $\bar{\delta} = \bar{u}_x + \bar{v}_y$ and the strain magnitude, $\bar{\alpha}^2 = (\bar{v}_y - \bar{u}_x)^2 + (\bar{v}_x + \bar{u}_y)^2$
 198 are both quantities that are invariant to a rotation of coordinate system and can be effectively treated
 199 as scalars. Clearly, in the limit of $\bar{\delta} \rightarrow 0$, the diagonal terms reduce to $\pm\bar{\alpha}/2$, so that the latter can
 200 also be referred to as the “non-divergent” strain though we drop the characterization in our usage
 201 here. In this rotated coordinate system the energy flux takes the form

$$\Pi_h = -[\tau_{uu}(\bar{\delta} + \bar{\alpha})/2 + \tau_{vv}(\bar{\delta} - \bar{\alpha})/2], \quad (6)$$

$$= (\tau_{vv} - \tau_{uu})\frac{\bar{\alpha}}{2} - (\tau_{vv} + \tau_{uu})\frac{\bar{\delta}}{2}, \quad (7)$$

$$= \underbrace{\mathcal{E}'\gamma\bar{\alpha}}_{\Pi_\alpha} - \underbrace{\mathcal{E}'\bar{\delta}}_{-\Pi_\delta}. \quad (8)$$

202 where $\mathcal{E}' = (\tau_{vv} + \tau_{uu})/2$ is the energy of finer scales, and $\bar{\delta}$ and $\bar{\alpha}$ are the divergence and strain of
 203 the coarse field. The parameter

$$\gamma \equiv \frac{\tau_{vv} - \tau_{uu}}{\tau_{vv} + \tau_{uu}} \quad (9)$$

204 is the anisotropy of finer scales in principal strain coordinates (Huang and Robinson 1998; Srinivasan and Young 2014). It is important to emphasize the coordinate system when discussing γ
 205 because unlike $\bar{\alpha}$, $\bar{\delta}$ and \mathcal{E}' , γ is not invariant to rotation. The term Π_α in related contexts is referred
 206 to as the deformation shear production (DSP) (Thomas 2012) but the Π_δ is new and is in general
 207 only relevant when $\bar{\delta}$ is significant i.e. for submesoscale currents and so we call it the convergence
 208 production (CP). Note that $-1 \leq \gamma \leq 1$ which gives the bounds $-\alpha\mathcal{E}' \leq \Pi_\alpha \leq \alpha\mathcal{E}'$. The expression
 209 in (8) can also be written in coordinate invariant form as
 210

$$\Pi_h = \underbrace{(\tau_{vv} - \tau_{uu})\frac{\bar{\sigma}_n}{2} - \tau_{uv}\bar{\sigma}_s}_{\Pi_\alpha} - \underbrace{(\tau_{vv} + \tau_{uu})\frac{\bar{\delta}}{2}}_{-\Pi_\delta}, \quad (10)$$

211 The Π_δ expectedly remains unchanged as it is the product of two coordinate invariant quantities,
 212 $\mathcal{E}' = (\tau_{vv} + \tau_{uu})/2$ and $\bar{\delta} = \bar{u}_x + \bar{v}_y$ but the two terms comprising Π_α associated with the normal
 213 strain, $\sigma_n = \bar{u}_x - \bar{v}_y$ and shear strain, $\sigma_s = \bar{u}_y + \bar{v}_x$ are not invariant and therefore have no separate
 214 meaning. While the principal strain form of Π_α in (8) has a very simple elegant form, estimating
 215 γ in principal strain coordinates is not straightforward and we mostly use the coordinate-free form
 216 specified in (10).

217 Eq. (10) with $\delta = 0$ was derived by Polzin (2010), for studying the interactions between IGWs
 218 and mesoscale flows, in straightforward fashion from (3). Even with $\delta \neq 0$, starting from (10) and
 219 showing that Π_h is equivalent to the form in (3) is easily done. However directly inferring the
 220 form of Π_h in (10) from (3) is not obvious and the principal strain coordinates helps arrive there
 221 naturally. The treatment of Π_h in principal strain coordinates outlined above follows that by Jing
 222 et al. (2017) in their study of near-inertial mesoscale eddy interactions, who derived the form in
 223 (7) for $\delta = 0$; in essence, $\Pi_h \propto \alpha$, where α is the mesoscale strain field. Our treatment extends the
 224 result to submesoscale flows for finite δ and we use it in the more general coarse-graining context.

225 *b. Frontogenetic equations*

226 The primary focus of this study is to examine the connection between energy transfer at fronts
 227 and frontogenesis. To this end we consider the evolution equation for the buoyancy gradient,
 228 $|\nabla b|^2 = b_x^2 + b_y^2$, also referred to as the frontogenetic tendency equation (Hoskins and Bretherton
 229 1972),

$$\frac{1}{2} \frac{D||\nabla b||^2}{Dt} = \underbrace{-(b_x^2 u_x + b_y^2 u_y) + b_x b_y (u_y + v_x)}_{\mathcal{B}_h} - \underbrace{b_z (w_x b_x + w_y b_y)}_{\mathcal{B}_v} \quad (11)$$

230 Then we can write (Barkan et al. 2019)

$$\mathcal{B}_h = -\mathbf{B} : \mathbf{S}, \quad (12)$$

231 where \mathbf{S} is the strain tensor while

$$\mathbf{B} = \begin{bmatrix} b_x^2 & b_x b_y \\ b_x b_y & b_y^2 \end{bmatrix} \quad (13)$$

232 is a *dyadic*, a special kind of second rank tensor formed by the outer product of two vectors, in
 233 this case of (b_x, b_y) with itself. Comparing (12) with (4) we note that the horizontal component
 234 of the buoyancy gradient tendency can be written in the same form as the horizontal component
 235 of the fine-scale energy tendency (4), with the fine scale stress tensor, $\boldsymbol{\tau}$ replaced by the buoyancy
 236 gradient tensor \mathbf{B} . As before we switch to the principal strain coordinates, and retracing the steps
 237 from (5) to (8) for (12) we get

$$\mathcal{B}_h = (|\nabla b|^2 \gamma_b \alpha - |\nabla b|^2 \delta) / 2. \quad (14)$$

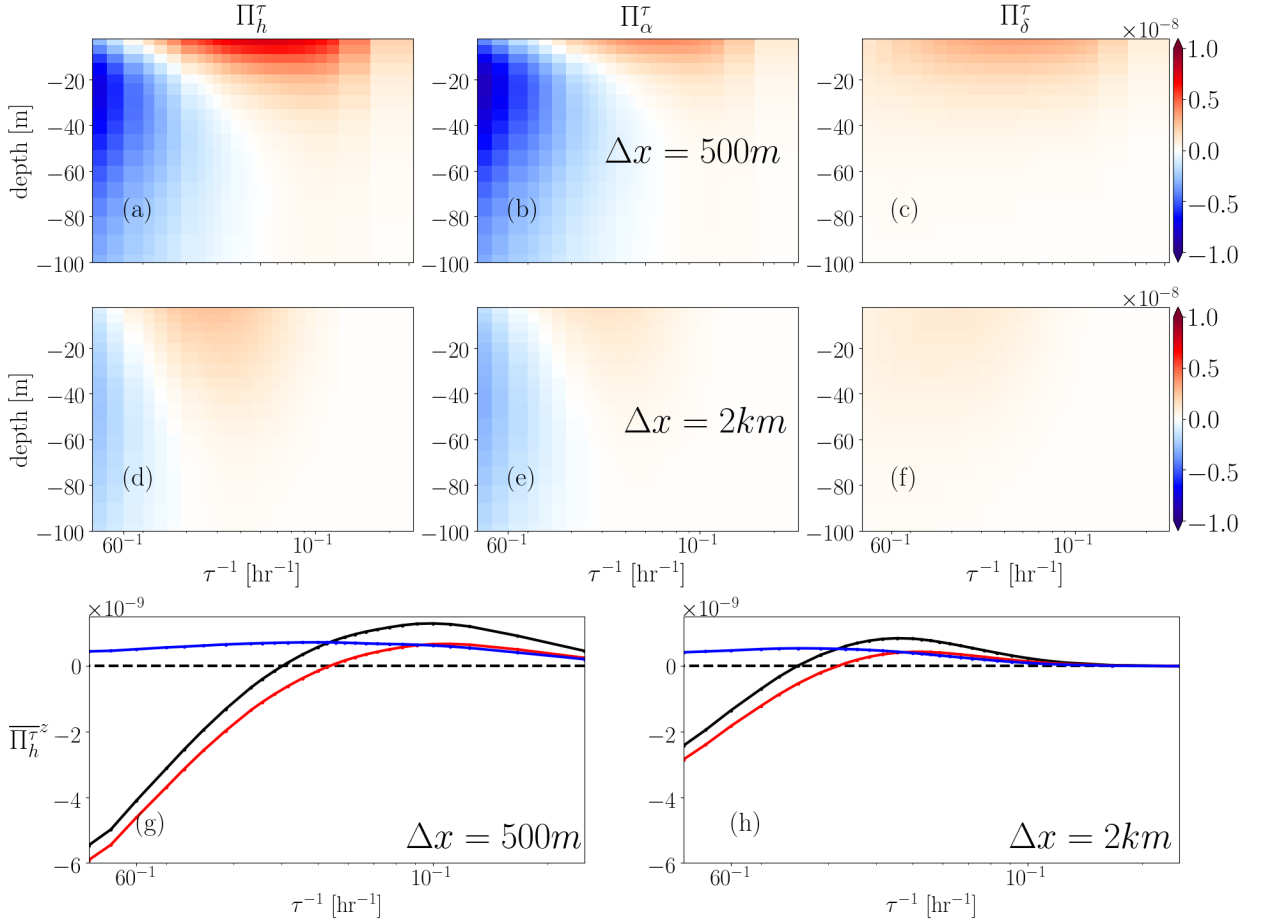
238 where γ_b is the buoyancy gradient anisotropy in principal strain coordinates

$$\gamma_b \equiv \frac{b_x^2 - b_y^2}{b_x^2 + b_y^2}, \quad (15)$$

239 and the coordinate free form of (14) in analogy with (10)

$$\mathcal{B}_h = \underbrace{(b_y^2 - b_x^2) \frac{\sigma_n}{2} - b_x b_y \sigma_s}_{B_\alpha} - \underbrace{(b_y^2 + b_x^2) \frac{\delta}{2}}_{-B_\delta}. \quad (16)$$

240 Recently (Balwada et al. 2021) derived the evolution equations for square of the gradient of a
 241 passive scalar ($|\nabla c|^2$) in principal strain coordinates, which is essentially the same as that of $|\nabla b|^2$
 242 derived above, although the authors do not express the result in the $\alpha - \delta$ form that we prefer
 243 or in the coordinate-free form in (16). In general, an equation like (16) can be written for any
 244 physical quantity whose rate of change takes the form in (12). Beyond scalar fields like b , we state
 245 (without elaboration) that similar forms can be written for the evolution equations of the square
 246 vertical shear, $u_z^2 + v_z^2$ [employed in the study of topographic submesoscale wakes (Srinivasan et al.
 247 2021) and front-surface wave interactions (Hypolite et al. 2021)] and the magnitude of the velocity
 248 gradient tensor, $|\nabla \mathbf{u}|^2$ [used as another proxy for frontogenesis by Barkan et al. (2019)]



251 FIG. 4. Horizontally and temporally averaged temporal energy fluxes [m^2s^{-3}] (a)-(f) as a function of depth
 252 and inverse filterscale [hr^{-1}] and (g), (h) vertically averaged over the top 50m. The top row shows fluxes at 500
 253 m resolution and the second row at 2 km resolution. The curves in the bottom row are the total horizontal flux
 254 $\overline{\Pi_h^\tau}$ (black), the deformation shear production Π_α^τ (red) and the convergence production Π_δ^τ (blue).

249 4. Results from the numerical model

250 a. Spatiotemporally averaged fluxes

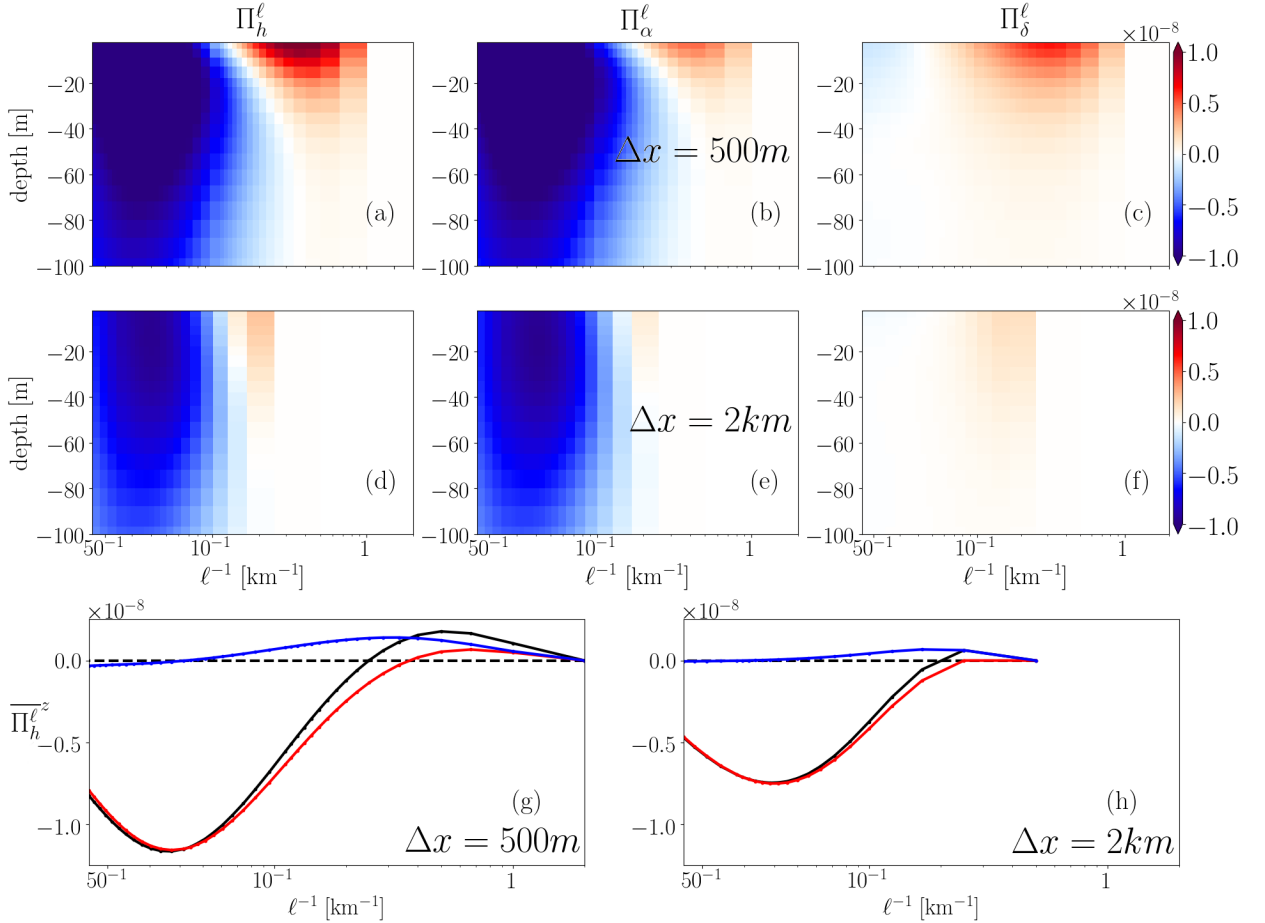
259 We compute the fluxes Π_h , Π_α and Π_δ from (10) at multiple depth levels between 0 and 100 m
 260 for two model runs at 2 km and 500 m resolutions. For each of the two runs and at each depth
 261 we use a range of scales for computing the fluxes - the spatial filter sizes are varied between the
 262 lowest grid scale (500 m and 2 km for the two models) to around 100 km while the temporal scales
 263 are varied between 1 hr and 100 hrs. Computing the fluxes on a cluster (XSEDE (Towns et al.

264 2014)) using the Ray multiprocessing library ¹ allows us to use a significantly larger number of
265 filters, 54 filters in space and 27 filters in time at a large number of depths, compared to recent
266 studies. The coarse-graining approach has the advantage over spectral methods in not needing a
267 windowing function for ensuring periodicity at the boundaries, but a consistent treatment of the
268 filter at the boundaries is still required. Whenever the spatial (uniform) filter hits the boundary, we
269 use a mirroring of the velocity field outward, preserving the structure of the flow. For the temporal
270 (Butterworth) filter, after filtering, we discarded the first 120 hours (being about twice the length of
271 the largest filter used) in January and last 120 hrs in March to avoid edge effects.

276 We first show Π_h , Π_α and Π_δ spatially averaged over the domain and temporally averaged over
277 the winter season (sans the edge data for the temporal case) in Figs. 4a-f (temporal transfer) and
278 5a-f (spatial transfer). These represent the average energy transferred over the whole domain and
279 during the winter months from scales larger to smaller. Thus positive values represent an energy
280 transfer to smaller scales (or a forward cascade) and negative values represent an inverse energy
281 cascade. Both figures show broadly similar patterns, in particular inverse cascade at larger (slower)
282 scales and forward cascade at smaller (faster) scales. The transition from forward to inverse transfer
283 is at 10km and around 50 hrs at the surface.

284 These transition scales need to be interpreted with some care given the different filter choices
285 in the two cases, the spatially sharp uniform filter and the spectrally sharp Butterworth filter in
286 time. To evaluate the importance of these filter choices on the flux, we also compute a temporal
287 scale-to-scale flux with the uniform filter at the surface and compare it with the flux obtained using
288 the Butterworth filter. Fig. 6 highlights the result that the forward-to-inverse transition timescale
289 obtained from the Butterworth filter is around 2.4 times larger than what one might expect from
290 the uniform filter flux calculation as demonstrated by plotting the flux obtained using the uniform
291 filter against 2.4τ instead of the actual filterscale, τ . Given the lack of an obvious implementation
292 of the Butterworth filter to two dimensions, we continue using the uniform filter, in line with recent
293 studies (Aluie et al. 2018; Schubert et al. 2020) with the knowledge that forward cascade region in
294 Fig. 5 occupies a larger range of scales and the actual transition scale is at a scale of 24km, rather
295 than 10km result found in Fig. 5. In particular, we introduce an equivalent spectral scale for the
296 spatial flux calculations $\lambda_{sp} = 2.4\ell$ and report it along with the actual filter scale ℓ . Later, in Sec. 6a
297 we again demonstrate the effective spectral resolution of the uniform filter, but by comparing

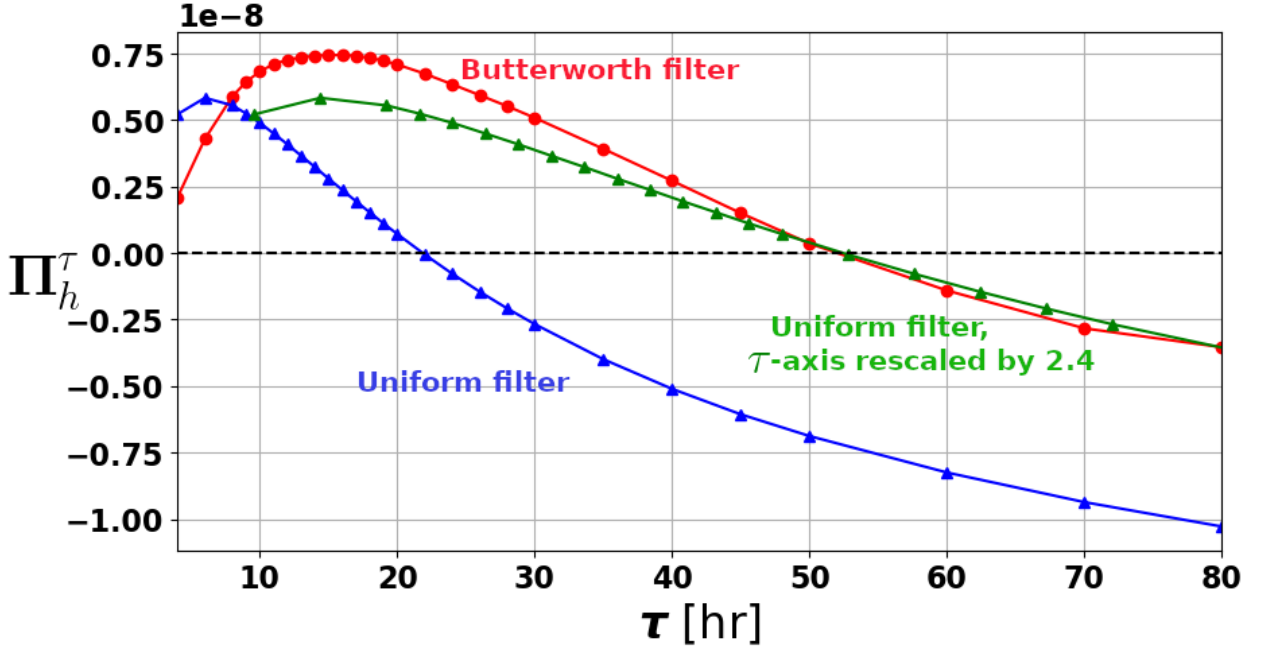
¹<https://github.com/ray-project/ray>



255 FIG. 5. Horizontally and temporally averaged spatial energy fluxes [m²s⁻³] (a)-(f) as a function of depth and
 256 inverse filterscale [km⁻¹] and (g), (h) vertically averaged over the top 50m. The top row shows fluxes at 500 m
 257 resolution and the second row at 2 km resolution. The curves in the bottom row are the total flux Π_h^ℓ (black), the
 258 deformation shear production Π_α^ℓ (red) and the convergence production Π_δ^ℓ (blue).

298 energy spectra instead of fluxes (see Fig. 13). A similar result was found by Schubert et al. (2020)
 299 by comparing the traditional spectral flux (in space) with the result from the coarse-grained fluxes
 300 from the uniform filter as done here although they obtained a factor of 2 instead of 2.4. We surmise
 301 that this is a consequence of the larger number of filters sizes used here, making it easier for us to
 302 estimate this factor accurately.

303 While the temporal transition scale is around 50 hr, a majority of the forward cascade (Figs. 4a
 304 and 6) is actually found within 24hr timescales. A recent study (Ajayi et al. 2021) computed
 305 (spatial) spectral energy fluxes at different regions of the North Pacific for a 1km resolution ocean



272 FIG. 6. Horizontally and temporally averaged temporal energy flux (Π_h^τ [m^2s^{-3}]) at the surface as a function of
 273 filterscale, τ [hr] for the choice of two filters, the Butterworth (red) and uniform (blue) filters. The green curve
 274 is simply the blue curve plotted against 2.4τ , i.e. by rescaling the abscissa by a factor of 2.4. The red curve is
 275 precisely the surface value in Fig. 4a although the abscissa here is τ instead of τ^{-1} .

306 model and found that using daily averages instead of snapshots substantially suppressed the forward
 307 energy cascade signal. Our temporal flux results explicate why this might be, assuming that in the
 308 absence of waves, the scales of motion associated with the temporal forward flux correspond to
 309 those that result in the spatial forward energy flux.

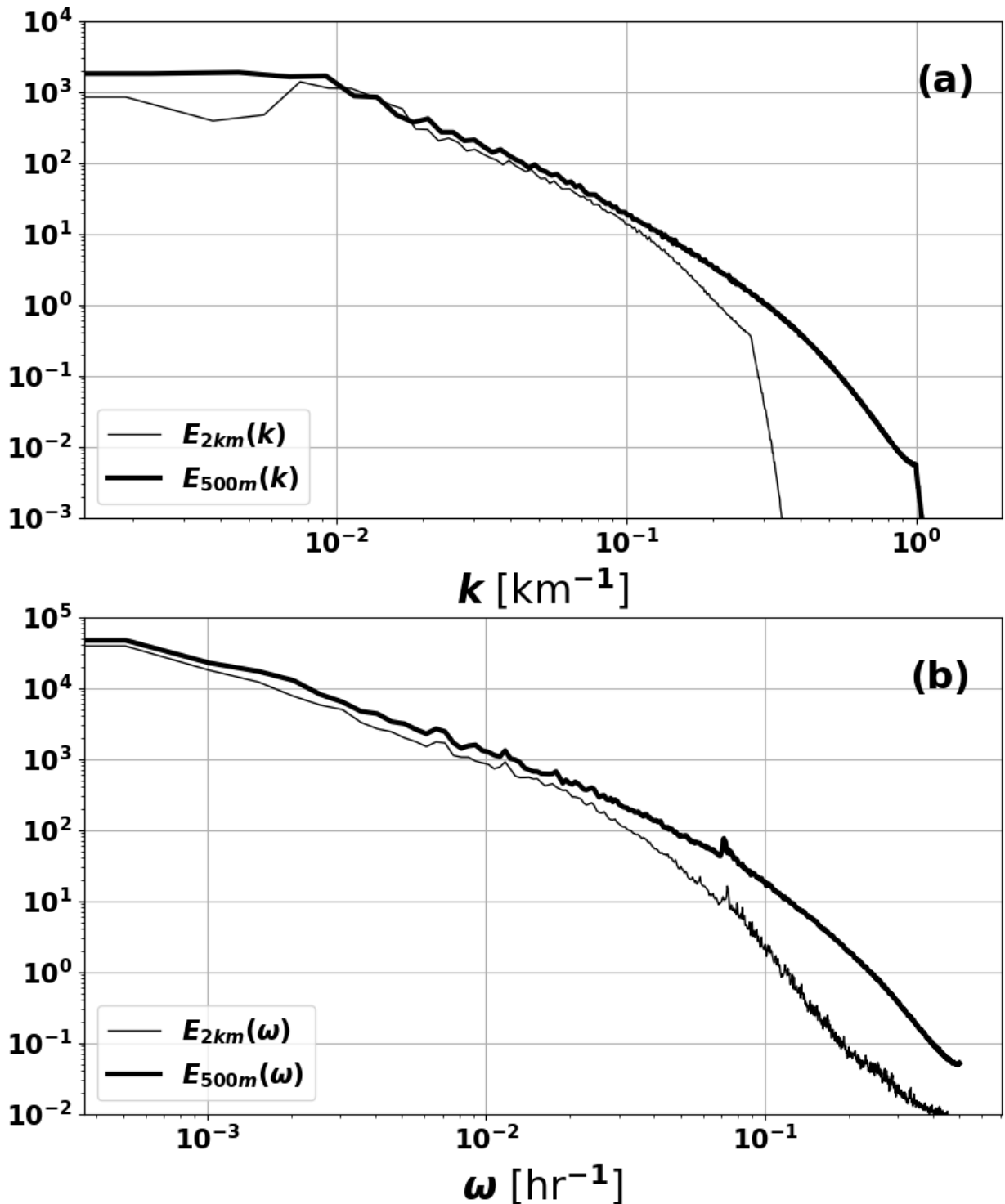
310 Both the forward and inverse cascade are weaker in the 2 km model run consistent with the
 311 notion that the 500 m model resolves both submesoscale MLEs and fronts better. The peak inverse
 312 energy flux is at $\ell=30$ km ($\lambda_{sp} = 72$ km) in the spatial though it is slower than the largest temporal
 313 filter width used here (i.e. slower than around 3 days which is still consistent with average MLE
 314 lifetimes of around a few days). In subsequent discussions we exclusively focus on the 500 m nest
 315 given the inadequacy of the 2 km nest in resolving submesoscales.

319 The most interesting results concern the breakup of Π_h into Π_α and Π_δ . Specifically, the inverse
 320 energy transfers in both the spatial and temporal cases are almost entirely due to the Π_α (or the DSP
 321 term); while the forward energy fluxes are approximately equipartitioned in the temporal case, the

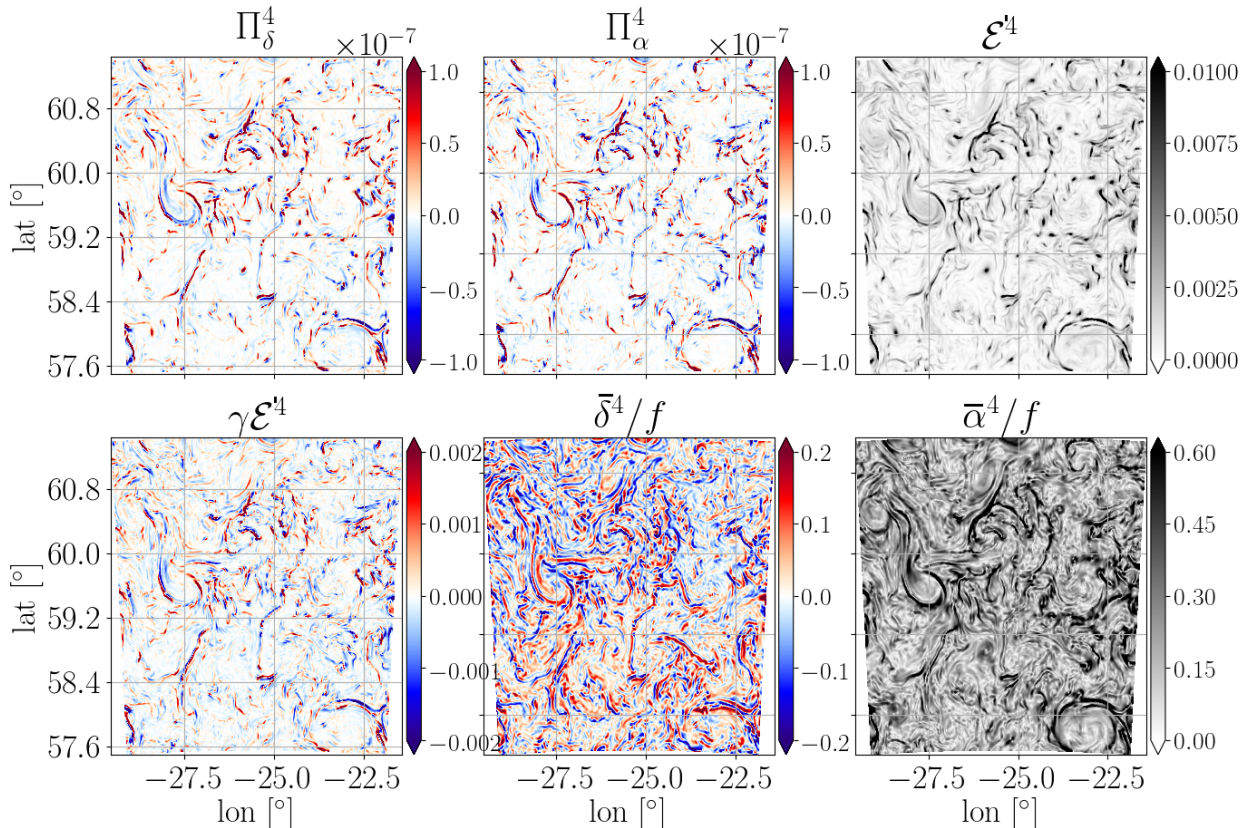
Π_δ (the CP term) is slightly larger in the spatial case. However, looking at the vertically integrated transfers, we notice that for scales smaller than 5 km ($\lambda_{sp} = 12$ km) and slower than around 10 hrs, both the Π_δ and the Π_α do in fact seem to converge, this being especially evident for the temporal case. We use the scaling for frontogenesis used in Barkan et al. (2019) to support the hypothesis that for small enough scales, there is an equipartition between Π_α and Π_δ . In general, the fact that the $\Pi_\delta = -\mathcal{E}'\delta$ is positive at the smallest, fastest scales is in line with our expectations about fronts, whose strong near-surface convergence (i.e. negative δ) should lead to positive values for Π_δ . This also offers clear evidence for the hypothesis by Capet et al. (2008b) that the forward energy cascade is due to ageostrophic motions (geostrophic flows have negligible δ). However the cause of the forward cascade contribution of Π_α are less clear. We plot the spatial and temporal energy spectra for the 2 km and 500 m winter runs (Fig. 7). Both show a larger level of energy at all scales in the 500 m model run relative to 2 km model. This is broadly consistent with the stronger inverse energy cascade in the 500 m model relative to the 2 km model from MLEs to larger scales. The 500 m model has a larger energy even at small scales in spite of having a stronger forward cascade. This is because both frontal dynamics and mixed layer instability are accompanied by a conversion of APE to KE, energizing the surface mixed layer. A quantitative explanation of the equilibrium structure of the energy spectrum would require a full spectral kinetic energy budget, which is not the focus here.

b. *The spatial structure of energy fluxes*

To shed greater light on the transfers, following Fig. 1, we visualize the spatial structure of Π_α and Π_δ in for different filter scales, along with the other components that constitute (8): $\bar{\alpha}$, $\bar{\delta}$, \mathcal{E}' and the principal strain anisotropy in the form $\gamma\mathcal{E}' = (\tau_{vv} - \tau_{uu})/2$. For a filter scale of $\ell = 4$ km ($\lambda_{sp} = 9.6$ km) we plot this breakup in Fig. 8. An immediate observation is the close similarity of the Π_α and Π_δ fields to the extent that they almost look identical at first glance. This further lends credence to the hypothesis that at frontal spatial scales, there is an approximate equipartition between the two terms. The largest positive values in the Π_α and Π_δ fields are found in regions where $\bar{\delta}$ is strongly negative (i.e. regions of strong convergence). The small scale kinetic energy is also collocated with the convergent regions, as is the anisotropy $\gamma\mathcal{E}'$ which suggests that that these two quantities are associated with the ageostrophic secondary circulation of the fronts, whose signature is the



316 FIG. 7. (a) Spatial [$\text{m}^2\text{s}^{-2}/(\text{cycles/m})$] and (b) temporal [$\text{m}^2\text{s}^{-2}/(\text{cycles/s})$] kinetic energy spectrum averaged
 317 over the winter months of January, February and March for the 2 km run (thin line) and the 500 m run (thick
 318 line).



341 FIG. 8. The same snapshot as Fig. 1 showing the various components of Equation (8): the convergence
 342 production, Π_{δ}^4 [m^2s^{-3}], the deformation shear production Π_{α}^4 , where the superscript indicates $\ell = 4$ km ($\lambda_{sp} = 9.6$
 343 km), i.e. Π^4 is the energy transferred from scales larger than 4 km to finer scales at a ocean surface. Also shown
 344 are the energy of the smaller scales \mathcal{E}^4 [m^2s^{-2}], the anisotropy of the final scales in the local principal strain
 345 coordinates $\gamma \mathcal{E}^4$, the larger scale divergence, $\bar{\delta}$ and the larger scale strain, $\bar{\alpha}$ normalized by the Coriolis paramter,
 346 f .

357 convergent region. The large scale strain $\bar{\alpha}$ also has a distinctly frontal structure but encompasses
 358 regions of both positive and negative divergence and has a broader extent than the other fields. It
 359 is important to keep in mind that this section explains the forward energy cascades at fronts purely
 360 based on the structure of fronts themselves; this is obvious in the case Π_{δ} but a little more nuanced
 361 in the case of Π_{α} . We provide a simple theoretical framework explaining this connection between
 362 the forward cascade at fronts and frontogenesis in the Sec. 5. The correspondence between Π_{α} and
 363 Π_{δ} breaks down at larger filter scales as is evident from Fig. 9 where a 12 km filter scale is used
 364 ($\lambda_{sp} = 28.8$ km). Π_{δ} is expectedly large where $\bar{\delta}$ is large and negative, however, Π_{α} is no longer

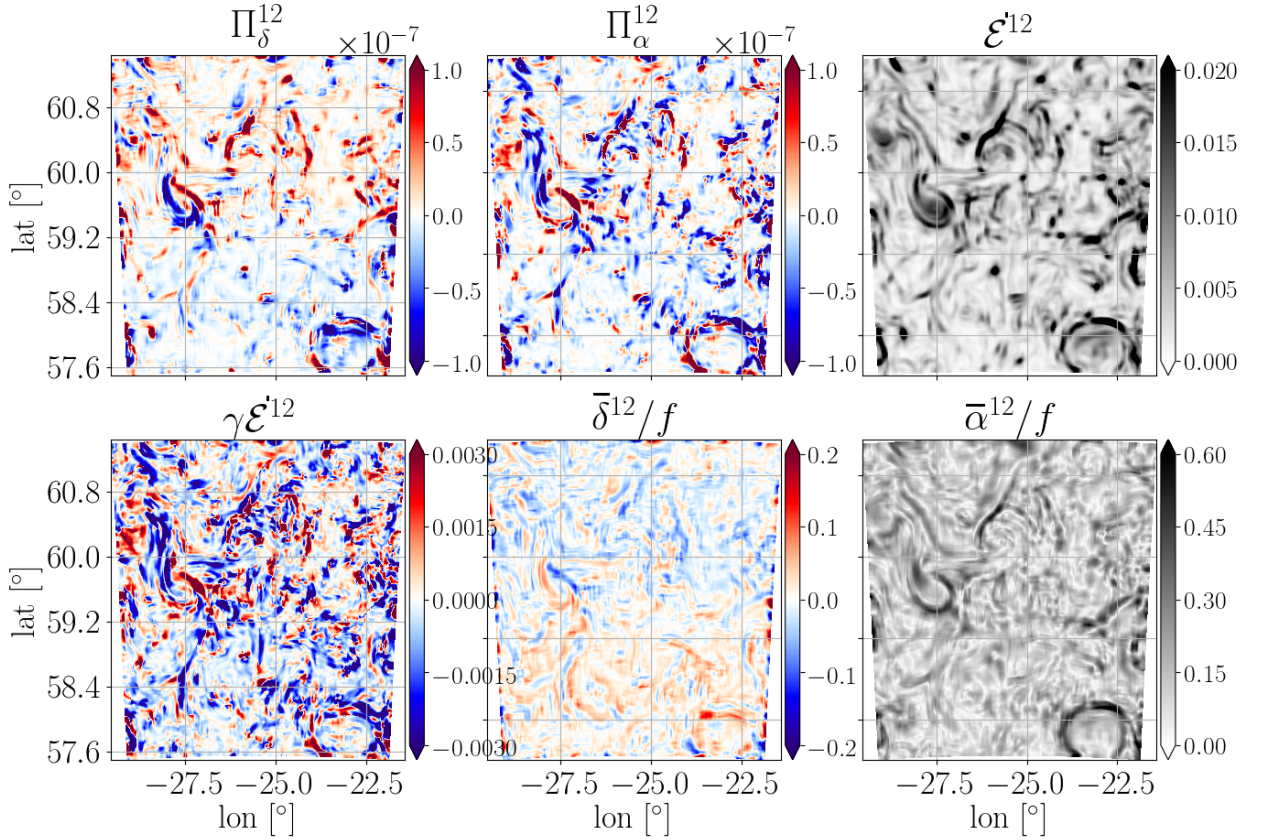


FIG. 9. Same as Fig. 8 but with a filter scale of $\ell = 12$ km ($\lambda_{sp} = 28.8$ km).

365 correlated with the same in spite of structural similarities between the two fields; at larger scales
 366 (i.e. at scales of MLEs), even these similarities in spatial patterns break down.

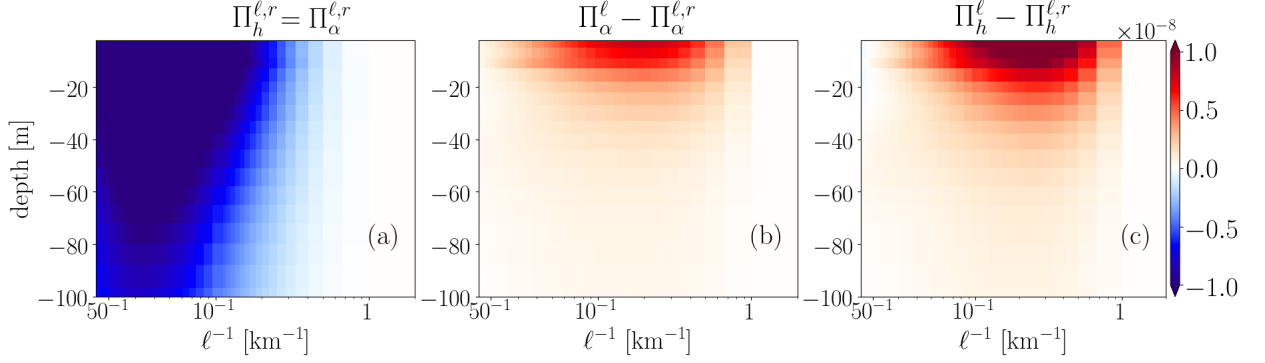
367 *c. Rotational and divergent components of the cross-scale energy flux*

368 Given that the Π_α and Π_δ terms do not cleanly separate mechanisms of inverse and forward energy
 369 fluxes, we decompose the horizontal velocity field into its rotational and divergent components,
 370 i.e. a Helmholtz decomposition, and subsequently compute energy transfers. Thus, we write

$$u = \phi_x + \psi_y, \quad (17)$$

$$v = \phi_y - \psi_x, \quad (18)$$

371 where ϕ and ψ are the velocity potential and streamfunction respectively. ϕ and ψ are solved by
 372 inverting the Poisson equations $\nabla^2 \phi = \delta$ and $\nabla^2 \psi = -\zeta$ assuming the simple Dirchlet boundary



382 FIG. 10. (a) Spatiotemporally averaged energy flux $\Pi_\alpha^{\ell,r}$ [m^2s^{-3}] ($=\Pi_h^{\ell,r}$) term computed purely using the
 383 rotational component of velocity. The corresponding $\Pi_\delta^{\ell,r}$ using only rotational components is trivially zero.
 384 (b) The difference between Π_α^ℓ and $\Pi_\alpha^{\ell,r}$ interpreted as the forward flux component of Π_α^ℓ . (c) The net forward
 385 energy flux component in Π_h^ℓ obtained by adding the result in (b) with that obtained in Fig. 5b; this is same as
 386 the difference between Π_h^ℓ and its purely rotational component, $\Pi_h^{\ell,r}$.

373 condition $\phi = 0$ at the boundary. We associate $(u_r, v_r) \equiv (\psi_y, -\psi_x)$ as the rotational component
 374 of the velocity and $(u_d, v_d) \equiv (\phi_y, \phi_x)$ as the divergent component. Note that once the Poisson
 375 equation for ϕ is inverted to obtain (u_d, v_d) , (u_r, v_r) are obtained by simply subtracting the divergent
 376 components from the full velocity field so that the Poisson equation for ψ does not actually need to
 377 be solved. To keep the analysis simple, we first compute the energy fluxes through (10) using *only*
 378 the rotational components i.e. both the constituent fine-scale stresses and the coarse-scale strains that
 379 make up the energy flux are entirely rotational. We refer to the resulting horizontal energy transfer
 380 as $\Pi_h^{\ell,r}$, where the superscript refers to “completely rotational”, noting that $\Pi_h^{\ell,r} = \Pi_\alpha^{\ell,r} + \Pi_\delta^{\ell,r}$.
 381 However, because $\Pi_\delta^\ell \propto \bar{\delta}$, we have that $\Pi_\delta^{\ell,r} \equiv 0$ and thus

$$\Pi_h^{\ell,r} = \Pi_\alpha^{\ell,r} \quad (19)$$

387 We plot the spatiotemporally averaged rotational component $\Pi_\alpha^{\ell,r}$ in Fig.10a and find it to be
 388 entirely upscale. The residual $\Pi_\alpha^\ell - \Pi_\alpha^{\ell,r}$ (Fig.10b) which includes a mix of rotational and divergent
 389 components, is almost entirely forward, implying that the purely rotation component, $\Pi_\alpha^{\ell,r}$ (equiv-
 390 alently $\Pi_h^{\ell,r}$ from (19)) accounts for the entirety of the inverse cascade of Π_h^ℓ . We associate this
 391 with the energetic interactions between MLEs through the mechanism demonstrated by Schubert
 392 et al. (2020) and also mesoscale eddies themselves. Adding this residual forward flux term to the

393 other forward flux term found earlier, Π_δ^ℓ (Fig. 5c) gives us the total forward flux associated with
 394 the flow and this works out to be

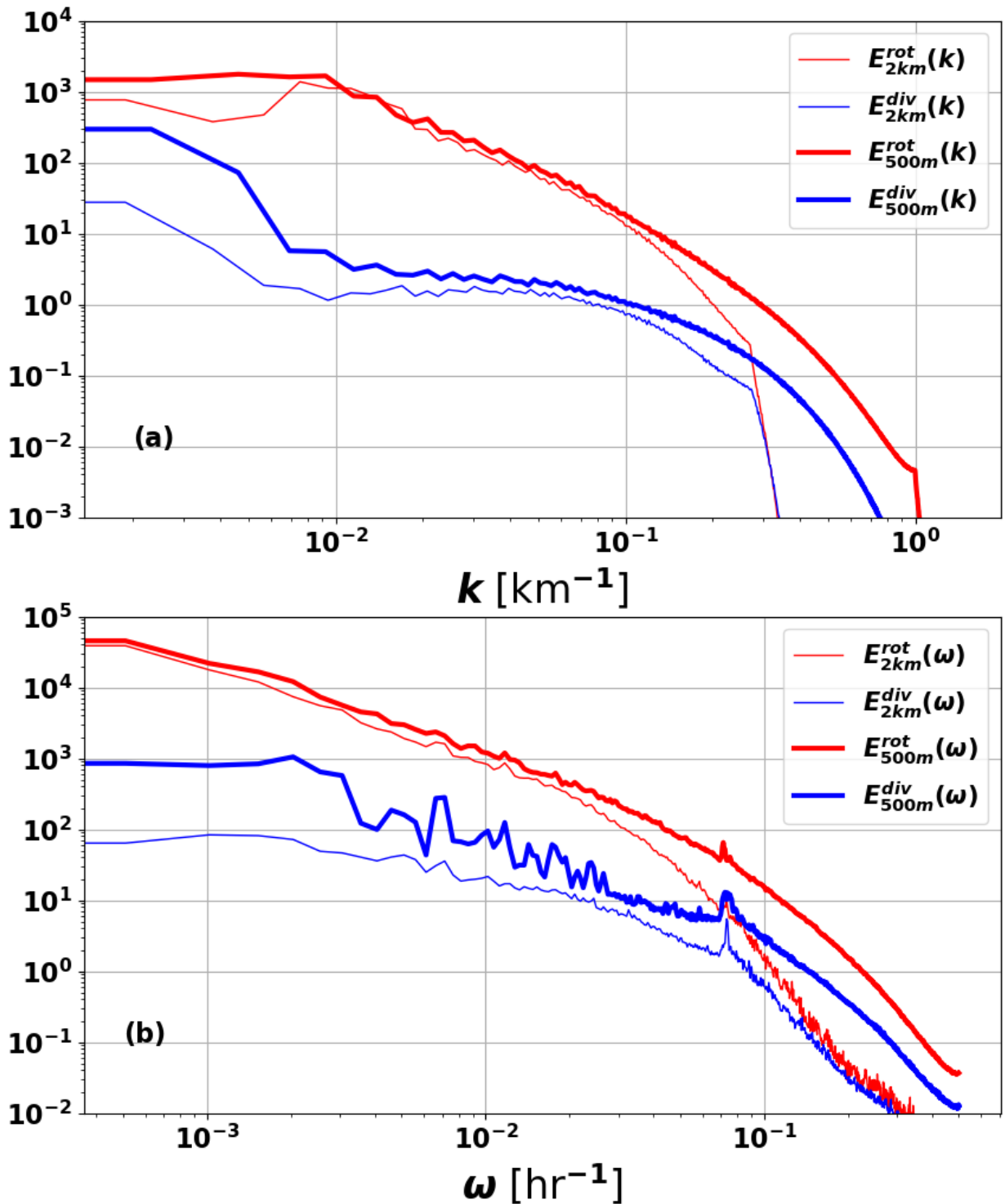
$$\Pi_\delta^\ell + \Pi_\alpha^\ell - \Pi_\alpha^{\ell,r} = \Pi_h^\ell - \Pi_h^{\ell,r} \quad (20)$$

398 where we used the fact that $\Pi_\delta^{\ell,r}$ is identically zero. The total forward flux is plotted in Fig. 10c.
 399 In summary, using the helmholtz decomposition, we can decompose the total horizontal transfer
 400 Π_h^ℓ into the inverse energy flux, given by $\Pi_h^{\ell,r}$ comprising interactions among purely rotational
 401 components and the forward energy flux $\Pi_h^\ell - \Pi_h^{\ell,r}$ which includes a mix of the rotational and
 402 divergent components. This decomposition is dynamically relevant unlike an attempted forward-
 403 inverse decomposition by Schubert et al. (2020) who separately average the negative values and
 404 positive values of Π_h^ℓ to separate the forward and inverse fluxes. It is notable that the peak values of
 405 the forward (Fig. 10c) and inverse (Fig. 10a) fluxes are in fact comparable though the latter spans a
 406 larger range of spatial scales and has a deeper vertical extent. The reason of course is that forward
 407 energy flux is highly localized at fronts. But a casual examination of the spatiotemporal energy
 408 spectra (Fig. 11a-b) of the divergent and rotational fields can give the impression that the divergent
 409 component is dynamically insignificant compared to the rotational (note the order of magnitude
 410 smaller spectral density at submesocales), in contrast with the picture that emerges from Fig. 10c.
 411 Though of secondary importance to the present study, a key question is how both the magnitude
 412 of the forward flux and the ratio of the rotational and divergent spectra change with increasing
 413 horizontal resolutions. We address this in detail in an upcoming study.

414 At this point it must be clear that the results in this section could have been obtained directly from
 415 (4) or (10) without employing the principle strain coordinates or the $\alpha - \delta$ decomposition; all that
 416 was required was the Helmholtz decomposition. However, the real strength of this decomposition
 417 lies in the theoretical connections that are readily established with the asymptotic framework for
 418 frontogenesis discovered by Barkan et al. (2019) as discussed in Section 5.

419 **5. The connection between energy flux at fronts and frontogenesis**

420 Barkan et al. (2019) provided a broad theoretical framework for frontogenesis based on general
 421 scaling considerations for frontal Rossby number, $Ro = V/fl$ and the frontal anisotropy, $\epsilon = l/L$,
 422 where V is the along front velocity scale and l the frontal width, and L the along front length scale.



395 FIG. 11. (a) Spatial [m²s⁻²/(cycles/m)] and (b) temporal kinetic energy spectrum [m²s⁻²/(cycles/s)] of the
 396 rotational (red lines) and divergent (blue lines) components of the flow averaged over the winter months of
 397 January, February and March for the 2 km (thin lines) and 500 m (thick lines) run.

423 Under the assumptions of

$$Ro \sim O(1), \quad \epsilon \ll 1, \quad (21)$$

424 both of which are defining frontal characteristics, Barkan et al. (2019) were able to show after
 425 neglecting dissipative terms, that for fronts ²,

$$\frac{D\delta}{Dt} \sim -\delta^2, \quad (22)$$

$$\frac{D\zeta}{Dt} \sim -\zeta\delta \quad (23)$$

$$\frac{D|\nabla b|^2}{Dt} \sim -2|\nabla b|^2\delta. \quad (24)$$

426 Eq. (22) can be solved directly in a Lagrangian reference frame and was shown by Barkan et al.
 427 (2019) to have a finite-time singularity similar to the result by Hoskins and Bretherton (1972)
 428 derived under the less general semi-geostrophic approximation. Of course, the actual singularity
 429 cannot manifest and the rapid increase in the convergence $-\delta$ is arrested in practice by frontal
 430 instabilities (like symmetric or shear instabilities), or numerical dissipation in ocean models. From
 431 (23) and (24), both ζ and ∇b also have finite-time singularities.

432 The equations for the fine-scale kinetic energy, from (8), can be written in the form (Aluie et al.
 433 2018),

$$\frac{D\mathcal{E}'}{Dt} + \nabla \cdot \mathcal{T} = -\bar{\delta}\mathcal{E}' + \gamma\mathcal{E}'\bar{\alpha} \quad (25)$$

434 where \mathcal{T} is the fine-scale kinetic energy transport flux (for detailed forms, see Aluie et al. (2018)
 435 or the Appendix B in Barkan et al. (2017)). The similarities in the dominant terms describing the
 436 evolution of $|\nabla b|^2$ and \mathcal{E}' as seen in (10) and (16) suggest that (25) can be written in a form similar
 437 to (24) under the frontal scalings (21). Here we neglect the vertical shear terms in both cases,
 438 which is justified in the scaling analysis of Barkan et al. (2019), supported by our model analysis;
 439 in particular Π_z [defined in (3)] is on average about 5 times smaller than Π_h (see Fig. 14). As
 440 a reminder, we note that while (25) involves coarse-grained quantities $\bar{\delta}$ and $\bar{\alpha}$, the frontogenetic
 441 equations (22)-(24) involve the actual fields themselves. Therefore these quantities are comparable
 442 in the limit when the filter-scale is smaller than the average frontal scale (in our case, $\ell \leq 10$ km or
 443 equivalently, $\lambda_{sp} \leq 24$ km).

²Two additional terms appear at leading order in the vorticity and divergence equations. These terms turn out to be subdominant as they cancel out with the vertical mixing terms through the turbulent thermal wind (TTW) balance that are not formally included in inviscid theory.

444 While the principal strain coordinates lead to very compact forms for the energy transfer, the
 445 Π_α term can be difficult to interpret, principally owing to the opaqueness of the anisotropy term
 446 γ . Instead, for the remainder of this section we work in a front aligned coordinate system, with
 447 the y -axis being along the frontal axis and x being the cross-frontal axis. The along and crossfront
 448 velocities are v and u respectively. Working in this coordinate system, we employ the coordinate-
 449 free forms of energy transfer (10) and frontogenetic tendency (16). The frontal scaling assumptions
 450 (21) need to be supplemented by one for the velocities,

$$u \sim Ro v. \quad (26)$$

451 which crucially differs from the semigeostrophic approximation of Hoskins and Bretherton (1972)
 452 who always have $u \ll v$. But because oceanic fronts have $Ro = O(1)$, $u \sim v$ i.e. the alongfront
 453 and crossfront velocities have similar order. This is a crucial observation about oceanic fronts
 454 that separates the analysis in Hoskins and Bretherton (1972) and Barkan et al. (2019). For frontal
 455 coarse graining scales, we also assume that the coarse and fine velocities scale similarly. i.e.

$$\bar{u} \sim \bar{v}, \quad u' \sim v'. \quad (27)$$

456 Thus we can infer that

$$\tau_{uu} \sim \tau_{vv} \sim \tau_{uv} \sim (\tau_{uu} + \tau_{vv})/2 = \mathcal{E}'. \quad (28)$$

457 Furthermore the crossfront gradients and alongfront gradients are related as

$$\partial_y \sim \epsilon \partial_x \Rightarrow \partial_y \ll \partial_x, \quad (29)$$

458 reflecting the crossfront gradients at fronts are a lot larger than alongfront gradients. From (29), we
 459 can infer that

$$\begin{aligned} \bar{\delta} &= \bar{u}_x + \bar{v}_y \\ &\sim \bar{u}_x \sim \bar{v}_x \\ &\sim \bar{v}_x - \bar{u}_y = \bar{\zeta}, \end{aligned} \quad (30)$$

460 i.e. $\bar{\delta} \sim \bar{\zeta}$ and that $\bar{\alpha}^2 \sim \bar{\delta}^2 + \bar{\zeta}^2$. Thus the strain comprises both divergent and rotational components.
 461 We can use the above scaling estimates to assess the energy transfer term Π_α using the coordinate
 462 free form (10). First to estimate Π_α ,

$$\begin{aligned}\Pi_\alpha &= (\tau_{uu} - \tau_{vv})(\bar{u}_x - \bar{v}_y)/2 - \tau_{uv}(\bar{u}_y + \bar{v}_x) \\ &\sim -\tau_{uv}\bar{v}_x/2 \sim -\mathcal{E}'\bar{u}_x \\ &\sim -\mathcal{E}'\bar{\delta} = \Pi_\delta,\end{aligned}\tag{31}$$

463 where we neglect the first term (because $\tau_{uu} \sim \tau_{vv}$) and the y-derivative in the second term (from
 464 (29)). Thus $\Pi_\alpha \sim \Pi_\delta$, supporting the model-based observation that Π_h has an equipartition at small
 465 scales. The scaling arguments used to infer this result fall short of an actual explanation for the
 466 striking similarity of the Π_α and Π_δ observed in Fig. 8 but provide a strong heuristic for the same.
 467 Then (25) can be written as

$$\frac{D\mathcal{E}'}{Dt} + \nabla \cdot \mathcal{T} \sim -2\bar{\delta}\mathcal{E}',\tag{32}$$

468 where we use $\Pi_\alpha \sim \Pi_\delta = -\mathcal{E}'\bar{\delta}$. Thus the evolution equation (32) takes the same form as (24).
 469 Because the equipartition demonstrated here is asymptotic, the precise numerical factor of 2
 470 multiplying $-\bar{\delta}\mathcal{E}'$ is not expected in general. In the simple model-based computation in Fig. 2, for
 471 example, the numerical factor is actually around 2.5 although that calculation depended on some
 472 specific choices for the frontal averaging which could affect the factor obtained. We also note
 473 the connection between the result obtained here, namely $-2\bar{\delta}\mathcal{E}'$ as the forward cascade at fronts,
 474 and that from the Helmholtz decomposition, $\Pi_h^\ell - \Pi_h^{\ell,r}$; the latter expression consists of a mix of
 475 rotational and divergent components which is consistent with the fact that although $\bar{\delta}$ is purely
 476 divergent, \mathcal{E}' comprises both rotational and divergent velocity fields.

477 For completeness, we derive (24) starting from the coordinate-free form in (16). From (29),
 478 using $b_y^2 \ll b_x^2$ and $b_x b_y \ll b_x^2$, we get

$$\begin{aligned}\mathcal{B}_\alpha &= (b_x^2 - b_y^2)(u_x - v_y)/2 - b_x b_y (u_y + v_x) \\ &\sim -b_x^2 u_x/2 \\ &\sim -(b_x^2 + b_y^2)\frac{\delta}{2} = \mathcal{B}_\delta,\end{aligned}\tag{33}$$

479 which leads to (24). Interestingly, as in the case of (31), (33) also demonstrates an equipartition in
480 the α and δ terms but the dominant terms are different. Now, because we associate the evolution
481 of ∇b through (24), it also follows that we associate the forward energy cascade at fronts as being
482 primarily caused due to frontogenesis. This is, in retrospect, expected because the rapid increase in
483 the convergence through (22) can be interpreted as a correspondingly rapid shrinkage in the frontal
484 scale, l associated with the frontal velocities, u and v . In other words, frontogenesis is the primary
485 cause of forward energy cascade at fronts.

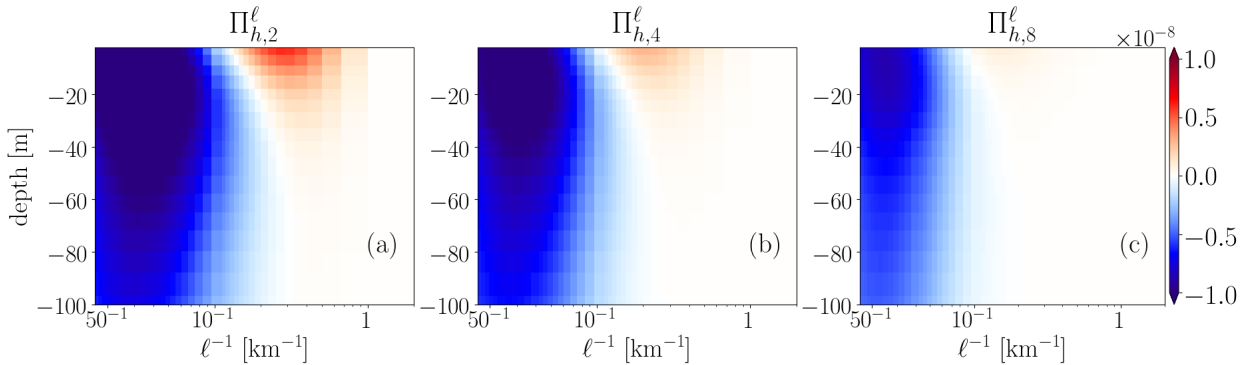
486 The mechanism elucidated above can be connected to the broader energetics of the surface mixed
487 layer as follows: Mixed layer instabilities which are strongest during the winter convert mixed layer
488 available potential energy to kinetic energy of fronts and MLEs. Frontogenesis transfers energy at
489 fronts to smaller scales by the mechanism proposed by Barkan et al. (2019) as demonstrated here,
490 while mixed layer eddies undergo an inverse cascade of energy to mesoscales as shown by Schubert
491 et al. (2020). Of course, this framing presumes that no competing mechanisms are present, chief
492 among them being symmetric instability which is likely not resolved at the 500 m model resolution
493 employed here. We discuss this last point further in Section 6b.

494 **6. Discussion**

495 *a. The dependence of energy transfer on effective flow resolution*

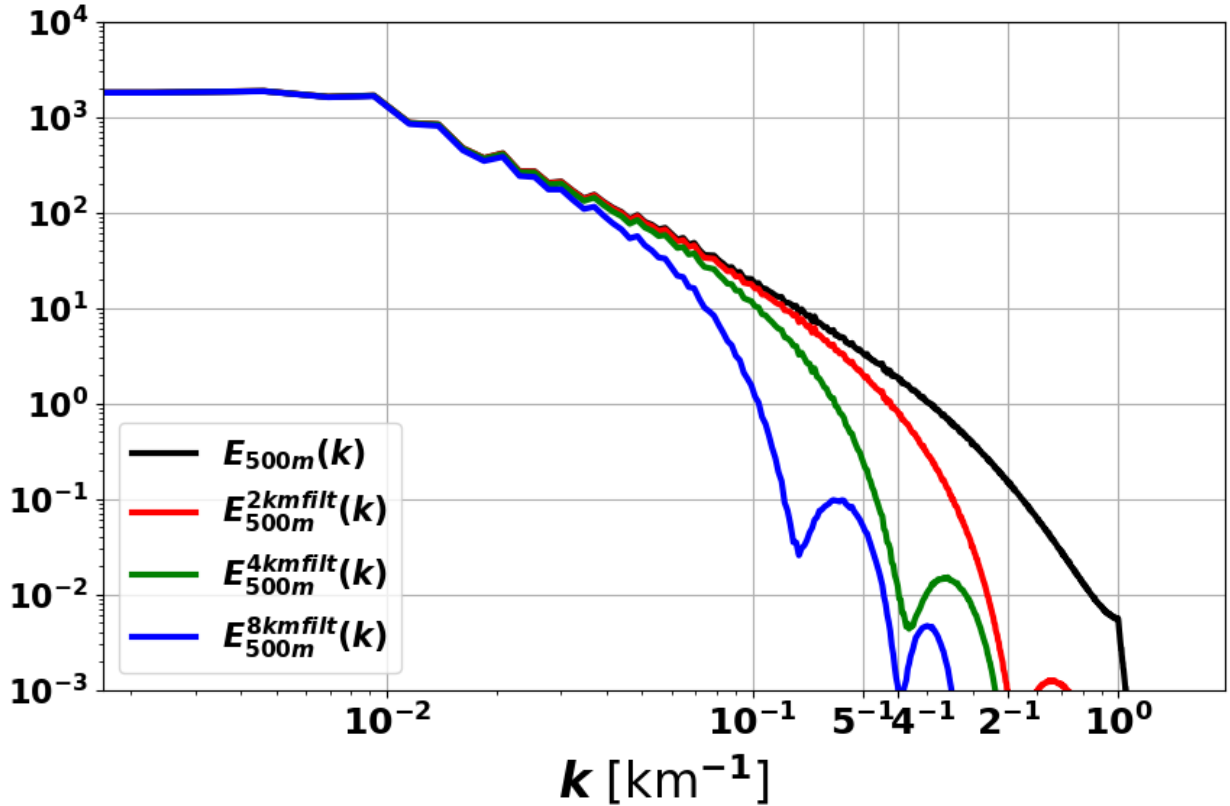
500 The 2 km solution, as seen in Figures 5 and 4 fails to not only resolve the forward cascade but
501 underestimates the submesoscale inverse cascade signal too. The reason for this is that the 2 km
502 model has a larger amount of numerical dissipation, which in ROMS is a grid dependent implicit
503 biharmonic dissipation i.e. lower resolutions are more dissipative and therefore can suppress
504 advective dynamics that lie closer to the grid resolution. Other studies have noted this increase
505 in upscale energy flux as the resolution is increased towards submesoscale-permitting resolutions
506 Kjellsson and Zanna (2017); Qiu et al. (2014). When computing energy transfers from observations,
507 however, the key issue is one of spatiotemporal resolution of the measured data (unlike models
508 where the issue is inaccurate physics). To study how spatial sampling affects the energy transfer
509 without the added effects of spurious physics (through higher numerical dissipation), we treat the
510 500 m run as the *ground truth* solution and smooth the flow fields with systematically larger filter
511 sizes and compute the crossscale energy fluxes of the smoothed fields. The actual fidelity of the 500

512 m run is not of particular importance; while it plausibly resolves the MLE inverse energy cascade accurately, it is likely that higher resolution runs would modify the forward energy flux.



496 FIG. 12. Spatiotemporally averaged horizontal energy flux [m^2s^{-3}] for the 500 m resolution run, with uniform
 497 smoothing performed on the velocity fields before computing the fluxes. The subscripts denote the smoothing
 498 filterwidth with values (a) 2 km (b) 4km and (c) 8km. These results are directly comparable to the unsmoothed
 499 energy transfer in Fig. 5a.

513
 519 Figure 12 shows the spatiotemporally averaged fluxes for increasing values of smoothing scale (a
 520 simple uniform filter is applied in each case). Comparing Fig. 12a, which has a 2 km smoothing,
 521 with the corresponding results from the 2 km model (Fig. 5d) and the 500 m model (Fig. 5a), we
 522 find that about half of the forward cascade and most of the inverse cascade region is accurately
 523 captured. The 4km smoothed fields have fluxes that resemble the 2 km model fluxes without a trace
 524 of the forward flux captured while the upscale flux is also diminished. The 8km smoothed fields
 525 (Fig. 12c) have almost no forward fluxes and substantially weaker upscale fluxes, suggesting that
 526 observations would need an average spatial resolution of at least 8km at this latitude to capture any
 527 fraction of the submesoscale energy fluxes. In Fig. 13 we also plot the spatial spectra corresponding
 528 to these smoothed fields. An interesting observation is the effect of the uniform filter on the spatial
 529 spectrum of the flow. For example, the 2km filter smoothed field has a rapid spectral drop off
 530 between 4 km and 5 km allowing us to infer that spectral cutoff is between 2 and 2.5 times the filter
 531 scale. However, it can be difficult to discern a single length scale as the effective spectral cutoff of
 532 the uniform filter given the continuous drop off starting from around 5 km scales of the 2km-filtered
 533 field (the red curve in Fig. 13). Unlike the spectrum however, the energy flux is a direct diagnostic



514 FIG. 13. (a) Spatial energy spectra [$\text{m}^2\text{s}^{-2}/(\text{cycles}/\text{m})$] of the velocity fields used to compute the energy flux
 515 for smoothing performed by different uniform filter sizes in Fig. 12. The red, green and blue curves correspond
 516 to Fig. 12a, b and c respectively. The black curve is the spectrum of the unsmoothed velocity field, replotted
 517 from Fig. 7a for reference. Note that the 2km-smoothed field (red) starts dropping off between 4 km and 5km
 518 scales.

534 of the dynamics allowing us to infer the effective spectral cutoff of the uniform filter, as has been
 535 done in Fig. 6 (Sec. 4a) where a factor of 2.4 was found.

536 *b. Symmetric instability: A competing and downstream mechanism for forward energy flux*

537 Symmetric Instability (SI) is a form of negative potential vorticity (PV) instability (Hoskins
 538 1974; Jones and Thorpe 1992; Thomas et al. 2013; Bachman and Taylor 2014; Yu et al. 2019)
 539 which occurs in the surface mixed layer when the potential vorticity of fronts is decreased through
 540 the action of surface wind stresses or diabatic cooling. Because frontal PV can be written as

541 (assuming geostrophic fronts)

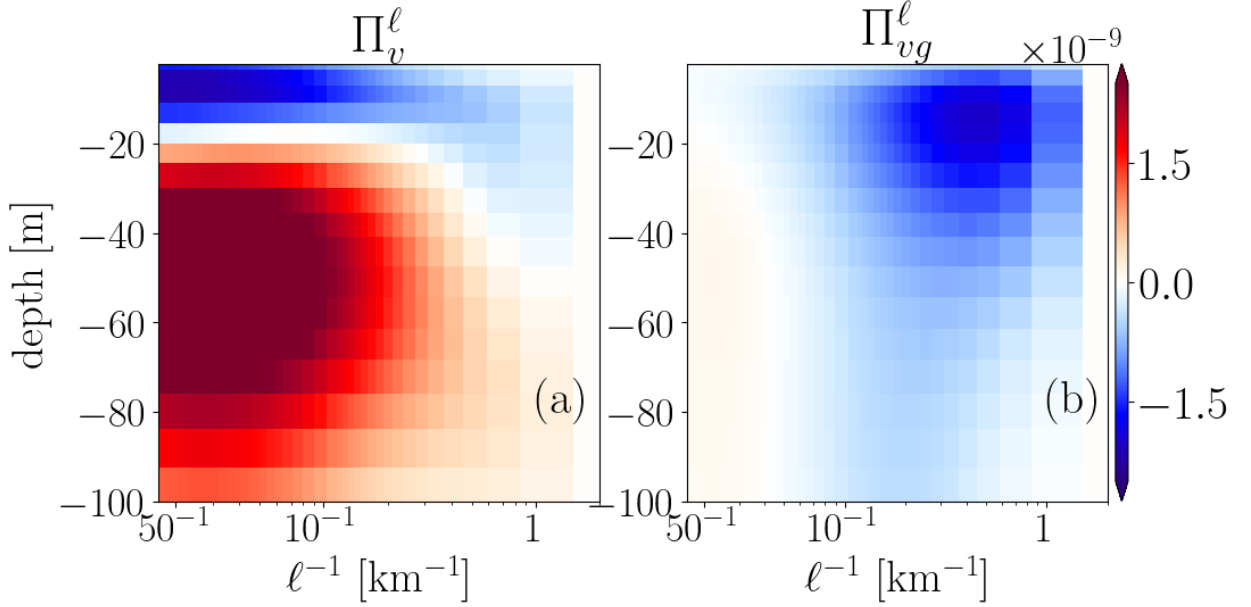
$$q = f(\zeta + f)b_z - |\nabla b|^2 \quad (34)$$

542 fronts with stronger buoyancy gradients are more likely to undergo SI. In the event that strong
 543 fronts do develop negative PV due to the action of surface forcing the front undergoes SI (referred
 544 specifically as *forced* SI), transferring energy to three-dimensional fine scale motions (i.e. a forward
 545 energy flux) through the vertical flux term Π_v^ℓ (more specifically the vertical flux term with the
 546 geostrophic coarse scale vertical shear, or the geostrophic shear production, GSP) in the process
 547 bringing the frontal PV to zero and restratifying the mixed layer.

548 Unlike the frontal forward mechanism demonstrated in this manuscript, SI is not a generic
 549 mechanism and depends crucially on the strength of fronts and the local surface forcing therein.
 550 For example a surface wind stress can generate negative PV fluxes through the so-called Ekman
 551 buoyancy fluxes but are strongly contingent on the direction of the wind stress relative to the front
 552 alignment; downfront winds being most favorable for inducing forced SI (Thomas and Lee 2005).
 553 Furthermore, the boundary layer turbulence mediated ageostrophic secondary circulation, also
 554 referred to as a turbulent thermal wind (TTW) balance (McWilliams et al. 2015; Wenegrat and
 555 McPhaden 2016; McWilliams 2017; Crowe and Taylor 2018), acts as a source of PV in the surface
 556 mixed layer which could potentially offset SI at oceanic fronts (Wenegrat et al. 2018). Given that
 557 the TTW mechanism is pervasive in submesoscale-resolving ocean models (McWilliams et al.
 558 2015; Wenegrat et al. 2018; Barkan et al. 2019), this could be a relevant offsetting mechanism for
 559 SI. In our present model runs, the vertical flux, Π_v^ℓ is on average 4 times smaller than Π_h^ℓ as is
 560 evident in Fig. 14a. Π_v^ℓ also has a rather different structure than Π_h^ℓ (Fig. 5a) with a forward flux
 561 close to the surface and a near-surface upscale flux. The spatiotemporally averaged geostrophic
 562 shear production,

$$\Pi_{vg}^\ell = -(\tau_{uw}\bar{u}_{z,g} + \tau_{vw}\bar{v}_{z,g}), \quad (35)$$

567 where $(\tau_{uw}, \tau_{vw}) \equiv (\overline{u\bar{w}} - \bar{u}\bar{w}, \overline{v\bar{w}} - \bar{v}\bar{w})$ are the vertical momentum fluxes and the coarse-scale
 568 geostrophic shear is $(\bar{u}_{z,g}, \bar{v}_{z,g}) \equiv (-\bar{b}_y, \bar{b}_x)/f$. Π_{vg}^ℓ is plotted as a function of ℓ in Fig. 14b and
 569 is largest at frontal scales but is *upscale* instead of *downscale* as might be expected if SI was a
 570 dominant process on average at these scales in our 500 m model run during winter. Note that
 571 this does not preclude the local importance of SI at strong density fronts with favorable wind



563 FIG. 14. Spatiotemporally averaged a) vertical shear energy flux, Π_v^ℓ [m^2s^{-3}] and b) the geostrophic shear
 564 production, Π_{vg}^ℓ , (defined in (35)) for the 500 m resolution run during winter months. Note that the colorbar
 565 ranges are 4 times smaller than the corresponding horizontal flux figures in the rest of this study. i.e. Π_v^ℓ is on
 566 average 4 times smaller than Π_h^ℓ .

572 stress. The structure of Π_v^ℓ (Fig. 14a) is likely a consequence of interactions between mesoscale
 573 and submesoscale eddies and IGWs (Barkan et al. 2021) and are not like the cascade processes that
 574 determine the structure of Π_h^ℓ . While IGWs in the present class of runs are rather weak, some level
 575 are likely present through the interaction of currents with bottom topography and the projection of
 576 the daily forced wind stress onto inertial motions. In the presence of wind and tide-generate IGWs,
 577 however, Π_v^ℓ is of similar order to Π_h^ℓ (Barkan et al. 2021).

578 Recently Dong et al. (2021b) studied an idealized front forced by downfront wind that subse-
 579 quently underwent SI. They found that in the absence of a SI-specific parameterization (Bachman
 580 et al. 2017) supplementing the surface boundary layer parameterization (in their case, as in ours,
 581 KPP) SI is suppressed and the GSP term is underestimated. We expect a similar lack of SI in our
 582 model results given the lack of an SI parameterization, an issue that we expect to remedy in future
 583 studies. Also, another recent paper (Dong et al. 2021a) used a global submesoscale permitting
 584 model solution to estimate the horizontal scale of SI in the ocean which would also correspond
 585 to the horizontal resolution at which SI could be potentially resolved in ocean models. They find

586 that in general, the resolutions required are below 100 m in a majority of the ocean, considerably
587 higher than the 500 m model used here. Although, concurrent work by (Jing et al. 2021) did find
588 evidence for SI along the fronts flanking the mesoscale eddies that formed part of the subtropical
589 countercurrent (STCC) during the summer (when the STCC eddies are most energetic) in the
590 Northwest Pacific, in a 500 m horizontal resolution model run. Because the STCC is a zonal
591 current, favorable downfront winds make the presence of SI in the summer in that region likely.
592 Whether such favorable surface forcing conditions exist in this region and their role in triggering
593 SI remains to be examined. Also of importance is the role of the mechanism of frontogenesis - in
594 summer mesoscale strain-induced frontogenesis is more likely to be important (as in the case of
595 STCC) whereas in winter mixed-layer instability in conjunction with TTW is more plausible; as
596 explained above, TTW can offset SI.

597 **7. Summary**

598 In this study we examine the flux of kinetic energy across spatial and temporal scales in subme-
599 soscale resolving simulations of the North Atlantic Ocean, focusing on the Iceland basin region.
600 Instead of the traditionally used spectral energy flux approach, we use the coarse-graining method
601 to compute the fluxes (Aluie et al. 2018). The coarse-graining approach involves a decomposition
602 of the flow into slow (large) and fast (small) components using a temporal (spatial) smoothing filter;
603 the equations for the kinetic energy of the coarse (large or slow) and fine (small or fast) components
604 are then written and the terms corresponding to the energy exchange (or equivalently the energy
605 flux from coarse to the fine scales) between the two components are identified. Following recent
606 work (Aluie et al. 2018; Schubert et al. 2020; Barkan et al. 2021), we analyze the cross-scale energy
607 flux in two ways. First, we average the flux over the horizontal domain and over the analysis time
608 period (here the winter months of January to March) and examine the average flux as a function
609 of filterscale and depth. Second, for specific filter scales and at a specific depth (here, near the
610 surface) we visualize the spatial structure of the flux and examine its patterns relative to observed
611 flow structures like mesoscale and mixed-layer eddies and submesoscale fronts. Our objective here
612 is to identify the nature of the cross-scale energy flux at $O(1-10)$ km length scales, that typically
613 correspond to submesoscale currents in the ocean, comprising mixed-layer eddies (MLEs) and

614 fronts that are generally limited to the near-surface mixed layer and particularly strong in the winter
615 months due to the presence of deep mixed layers.

616 A plethora of studies over the past two decades, starting from Capet et al. (2008b) have found that
617 submesoscales have a dual cascade of energy, an inverse cascade to mesoscale eddies and a forward
618 energy cascade to dissipation scales. Recent work by Schubert et al. (2020) also employing the
619 coarse-graining approach used here, were able to show that MLEs undergo an inverse cascade of
620 energy to mesoscales, in particular providing a visual demonstration of the ‘absorption’ of MLEs
621 into mesoscale eddies. They also highlighted a forward energy flux at fronts without providing a
622 physical explanation for this phenomenon. In this study we provide the mechanism for the frontal
623 forward cascade through model-based analysis and by extending a recently proposed asymptotic
624 theory for frontogenesis (Barkan et al. 2019).

625 In order to shed light on the mechanism of the frontal forward flux we pursue two concurrent
626 approaches building on the coarse-graining framework. First we decompose the flow field into
627 rotational and divergent components i.e. a Helmholtz decomposition. We then compute the
628 cross-scale flux purely due to the rotational velocity components. This rotational flux is found,
629 on spatio-temporal averaging, to be almost entirely upscale (i.e. an inverse cascade) in the upper
630 ocean. The difference between the total flux and the rotational flux is found to be, on average,
631 entirely downscale (i.e. a forward cascade). In other words the Helmholtz decomposition neatly
632 decomposes the inverse and forward energy flux components of the flow.

633 Concurrently, we write the cross-scale energy flux in the principal strain coordinates, where the
634 coarse (or smoothed by the filter) field strain tensor is diagonalized. This allows the flux to be
635 written in a simple sum of two components where the first component is proportional to the coarse
636 strain, $\bar{\alpha}$ and the second component is proportional to the convergence (i.e. negative divergence) of
637 the coarse field, $-\bar{\delta}$, where $(\bar{\cdot})$ denotes the filter-based smoothing operator. Calculating these two
638 components in the model data, we find that the $\bar{\alpha}$ component consists (on average) of most of the
639 inverse energy flux but the total forward flux is equipartitioned between the $\bar{\alpha}$ and $\bar{\delta}$ components. We
640 then use the asymptotic theory of frontogenesis proposed by Barkan et al. (2019) to theoretically
641 demonstrate the equipartition of the forward energy flux at fronts between the $\bar{\alpha}$ and $\bar{\delta}$ terms
642 (Section 5) for fronts. But this equipartition also means that, because the $\bar{\delta}$ component of flux
643 is proportional to the convergence, $-\bar{\delta}$, so is the $\bar{\alpha}$ component and consequently so is the total

644 energy flux at fronts (which is just a sum of the two components). Note that because fronts are
645 convergent flows ($\delta < 0$), this essentially provides a theoretical and numerical basis for the forward
646 energy flux at fronts. Furthermore, in the asymptotic theory of frontogenesis by Barkan et al.
647 (2019), a crucial result was that the Lagrangian rate of change (i.e. D/Dt) of frontal quantities
648 like vorticity, divergence and buoyancy gradient were all proportional to $-\delta$ which at fronts is
649 positive. This causes a finite time singularity in the convergence and correspondingly in the other
650 frontal quantities i.e. frontogenesis. The fact that the rate of change of the fine scale kinetic energy,
651 i.e. the cross-scale energy flux is also proportional to $-\bar{\delta}$ allows us to infer that the cause of the
652 forward energy flux at fronts is actually frontogenesis (noting that δ and $\bar{\delta}$ are similar when the
653 coarse-graining scale is around frontal scales). Heuristically this is because the sharpening of
654 fronts due to frontogenesis essentially transfers the frontal energy to smaller scales resulting in a
655 forward energy flux.

656 *Acknowledgments.* Kaushik Srinivasan, Roy Barkan and James C. McWilliams were supported
657 by ONR-N000141812697. Roy Barkan was further supported by NSF Grant OCE-1851397 and
658 Israeli Science foundation Grant 1736/18. James C. McWilliams was further supported ONR-
659 N000141812599 and ONR N000142012023. Computation of model simulations and most of the
660 scale-to-scale analysis used here was performed on Extreme Science and Engineering Discovery
661 Environment (XSEDE) clusters (Towns et al. 2014).

662 *Data availability statement.* The 2 km and 500 m ROMS-based North Atlantic simulations used
663 in this study are not publicly archived but can be made available through direct requests to the
664 corresponding author. The CFSR reanalysis product (Saha et al. 2014; Dee et al. 2014) used to
665 force the ROMS simulation can be found at Saha et al. (2012).

666 **References**

- 667 Ajayi, A., J. Le Sommer, E. P. Chassignet, J.-M. Molines, X. Xu, A. Albert, and W. Dewar,
668 2021: Diagnosing cross-scale kinetic energy exchanges from two submesoscale permitting
669 ocean models. *Journal of Advances in Modeling Earth Systems*, e2019MS001923.
- 670 Alford, M. H., J. A. MacKinnon, H. L. Simmons, and J. D. Nash, 2016: Near-inertial internal
671 gravity waves in the ocean. *Annual review of marine science*, **8**, 95–123.

- 672 Aluie, H., M. Hecht, and G. K. Vallis, 2018: Mapping the energy cascade in the North Atlantic
673 Ocean: The coarse-graining approach. *J. Phys. Oceanogr.*, **48** (2), 225–244.
- 674 Bachman, S. D., B. Fox-Kemper, J. R. Taylor, and L. N. Thomas, 2017: Parameterization of frontal
675 symmetric instabilities. i: Theory for resolved fronts. *Ocean Modelling*, **109**, 72–95.
- 676 Bachman, S. D., and J. R. Taylor, 2014: Modelling of partially-resolved oceanic symmetric
677 instability. *Ocean Modelling*, **82**, 15–27.
- 678 Balwada, D., Q. Xiao, S. Smith, R. Abernathey, and A. R. Gray, 2021: Vertical fluxes conditioned
679 on vorticity and strain reveal submesoscale ventilation. *Journal of Physical Oceanography*.
- 680 Barkan, R., M. J. Molemaker, K. Srinivasan, J. C. McWilliams, and E. A. D’Asaro, 2019: The role
681 of horizontal divergence in submesoscale frontogenesis. *Journal of Physical Oceanography*,
682 **49** (6), 1593–1618.
- 683 Barkan, R., K. Srinivasan, L. Yang, , J. C. McWilliams, J. Gula, and C. Vic, 2021: Oceanic cross-
684 scale energy transfers under the influence of internal waves. *Geophysical Research Letters*, **0** (0),
685 10–20.
- 686 Barkan, R., K. B. Winters, and J. C. McWilliams, 2017: Stimulated imbalance and the enhancement
687 of eddy kinetic energy dissipation by internal waves. *J. Phys. Oceanogr.*, **47** (1), 181–198.
- 688 Barkan, R., K. B. Winters, and S. G. L. Smith, 2015: Energy cascades and loss of balance in a
689 reentrant channel forced by wind stress and buoyancy fluxes. *Journal of Physical Oceanography*,
690 **45** (1), 272–293.
- 691 Boccaletti, G., R. Ferrari, and B. Fox-Kemper, 2007: Mixed layer instabilities and restratification.
692 *J. Phys. Oceanogr.*, **37** (9), 2228–2250.
- 693 Brannigan, L., D. P. Marshall, A. Naveira-Garabato, and A. G. Nurser, 2015: The seasonal cycle
694 of submesoscale flows. *Ocean Modell.*, **92**, 69–84.
- 695 Callies, J., R. Ferrari, J. M. Klymak, and J. Gula, 2015: Seasonality in submesoscale turbulence.
696 *Nat. Commun.*, **6**, 6862.
- 697 Callies, J., G. Flierl, R. Ferrari, and B. Fox-Kemper, 2016: The role of mixed-layer instabilities in
698 submesoscale turbulence. *Journal of Fluid Mechanics*, **788**, 5–41.

- 699 Capet, X., P. Klein, B. L. Hua, G. Lapeyre, and J. C. McWilliams, 2008a: Surface kinetic energy
700 transfer in surface quasi-geostrophic flows. *Journal of Fluid Mechanics*, **604**, 165–174.
- 701 Capet, X., J. C. McWilliams, M. J. Molemaker, and A. F. Shchepetkin, 2008b: Mesoscale to
702 submesoscale transition in the California Current System. Part III: Energy balance and flux. *J.*
703 *Phys. Oceanogr.*, **38**, 44–64, doi:10.1175/2008JPO3810.1.
- 704 Crowe, M. N., and J. R. Taylor, 2018: The evolution of a front in turbulent thermal wind balance.
705 part 1. theory. *Journal of Fluid Mechanics*, **850**, 179–211.
- 706 Dee, D., M. Balmaseda, G. Balsamo, R. Engelen, A. Simmons, and J.-N. Thépaut, 2014: Toward
707 a consistent reanalysis of the climate system. *Bulletin of the American Meteorological Society*,
708 **95** (8), 1235–1248.
- 709 Dong, J., B. Fox-Kemper, H. Zhang, and C. Dong, 2021a: The scale and activity of symmetric
710 instability estimated from a global submesoscale-permitting ocean model. *Journal of Physical*
711 *Oceanography*, **51** (5), 1655–1670.
- 712 Dong, J., B. Fox-Kemper, J. Zhu, and C. Dong, 2021b: Application of symmetric instability pa-
713 rameterization in the coastal and regional ocean community model (croco). *Journal of Advances*
714 *in Modeling Earth Systems*, **13** (3), e2020MS002302.
- 715 Eyink, G. L., and H. Aluie, 2009: Localness of energy cascade in hydrodynamic turbulence. I.
716 Smooth coarse graining. *Phys. of Fluids*, **21** (11), 115–107.
- 717 Ferrari, R., and C. Wunsch, 2009: Ocean circulation kinetic energy: Reservoirs, sources, and
718 sinks. *Annual Review of Fluid Mechanics*, **41**.
- 719 Garabato, A. C. N., X. Yu, J. Callies, R. Barkan, K. L. Polzin, E. E. Frajka-Williams, C. E. Buck-
720 ingham, and S. M. Griffies, 2022: Kinetic energy transfers between mesoscale and submesoscale
721 motions in the open ocean’s upper layers. *Journal of Physical Oceanography*, **52** (1), 75–97.
- 722 Hoskins, B., 1974: The role of potential vorticity in symmetric stability and instability. *Quarterly*
723 *Journal of the Royal Meteorological Society*, **100** (425), 480–482.
- 724 Hoskins, B. J., and F. P. Bretherton, 1972: Atmospheric frontogenesis models: Mathematical
725 formulation and solution. *J. Atmos. Sci.*, **29** (1), 11–37.

726 Huang, H.-P., and W. A. Robinson, 1998: Two-dimensional turbulence and persistent zonal jets in
727 a global barotropic model. *Journal of the atmospheric sciences*, **55** (4), 611–632.

728 Hypolite, D., L. Romero, J. C. McWilliams, and D. P. Dauhajre, 2021: Surface gravity wave
729 effects on submesoscale currents in the open ocean. *Journal of Physical Oceanography*, **51** (11),
730 3365–3383.

731 Jing, Z., B. Fox-Kemper, H. Cao, R. Zheng, and Y. Du, 2021: Submesoscale fronts and their
732 dynamical processes associated with symmetric instability in the northwest pacific subtropical
733 ocean. *Journal of Physical Oceanography*, **51** (1), 83–100.

734 Jing, Z., L. Wu, and X. Ma, 2017: Energy exchange between the mesoscale oceanic eddies and
735 wind-forced near-inertial oscillations. *Journal of Physical Oceanography*, **47** (3), 721–733.

736 Jones, S. C., and A. J. Thorpe, 1992: The three-dimensional nature of ‘symmetric’ instability.
737 *Quarterly Journal of the Royal Meteorological Society*, **118** (504), 227–258.

738 Kjellsson, J., and L. Zanna, 2017: The impact of horizontal resolution on energy transfers in global
739 ocean models. *Fluids*, **2** (3), 45.

740 Klein, P., B. L. Hua, G. Lapeyre, X. Capet, S. Le Gentil, and H. Sasaki, 2008: Upper ocean
741 turbulence from high-resolution 3d simulations. *Journal of Physical Oceanography*, **38** (8),
742 1748–1763.

743 Klein, P., and Coauthors, 2019: Ocean-scale interactions from space. *Earth and Space Science*,
744 **6** (5), 795–817.

745 Leonard, A., 1975: Energy cascade in large-eddy simulations of turbulent fluid flows. *Advances in*
746 *geophysics*, Vol. 18, Elsevier, 237–248.

747 Ma, X., and Coauthors, 2016: Western boundary currents regulated by interaction between ocean
748 eddies and the atmosphere. *Nature*, **535** (7613), 533–537.

749 McWilliams, J. C., 2016: Submesoscale currents in the ocean. *Proc. R. Soc. A*, The Royal Society,
750 Vol. 472, 20160117.

751 McWilliams, J. C., 2017: Submesoscale surface fronts and filaments: Secondary circulation,
752 buoyancy flux, and frontogenesis. *Journal of Fluid Mechanics*, **823**, 391.

- 753 McWilliams, J. C., J. Gula, M. J. Molemaker, L. Renault, and A. F. Shchepetkin, 2015: Filament
754 frontogenesis by boundary layer turbulence. *J. Phys. Oceanogr.*, **45** (8), 1988–2005.
- 755 Mensa, J. A., Z. Garraffo, A. Griffa, T. M. Özgökmen, A. Haza, and M. Veneziani, 2013: Sea-
756 sonality of the submesoscale dynamics in the Gulf Stream region. *Ocean Dynamics*, **63** (8),
757 923–941.
- 758 Molemaker, M. J., J. C. McWilliams, and X. Capet, 2010: Balanced and unbalanced routes to
759 dissipation in an equilibrated Eady flow. *J. Fluid Mech.*, **654**, 33–63.
- 760 Polzin, K. L., 2010: Mesoscale eddy–internal wave coupling. part ii: Energetics and results from
761 polymode. *Journal of physical oceanography*, **40** (4), 789–801.
- 762 Qiu, B., S. Chen, P. Klein, H. Sasaki, and Y. Sasai, 2014: Seasonal mesoscale and subme-
763 soscale eddy variability along the north pacific subtropical countercurrent. *Journal of Physical*
764 *Oceanography*, **44** (12), 3079–3098.
- 765 Rai, S., M. Hecht, M. Maltrud, and H. Aluie, 2021: Scale of oceanic eddy killing by wind from
766 global satellite observations. *Science Advances*, **7** (28), eabf4920.
- 767 Renault, L., P. Marchesiello, S. Masson, and J. C. Mcwilliams, 2019: Remarkable control of
768 western boundary currents by eddy killing, a mechanical air-sea coupling process. *Geophysical*
769 *Research Letters*, **46** (5), 2743–2751.
- 770 Renault, L., J. C. McWilliams, and J. Gula, 2018: Dampening of submesoscale currents by air-sea
771 stress coupling in the californian upwelling system. *Scientific reports*, **8** (1), 1–8.
- 772 Renault, L., M. J. Molemaker, J. C. McWilliams, A. F. Shchepetkin, F. Lemarié, D. Chelton,
773 S. Illig, and A. Hall, 2016: Modulation of wind work by oceanic current interaction with the
774 atmosphere. *Journal of Physical Oceanography*, **46** (6), 1685–1704.
- 775 Rocha, C. B., G. L. Wagner, and W. R. Young, 2018: Stimulated generation: extraction of energy
776 from balanced flow by near-inertial waves. *Journal of Fluid Mechanics*, **847**, 417–451.
- 777 Saha, S., and Coauthors, 2012: NCEP climate forecast system version 2 (CFSR) selected hourly
778 time-series products, January 1979 to December 2010. *Research Data Archive at the National*

779 Center for Atmospheric Research, Computational and Information Systems Laboratory, **10**,
780 D6513W89, <https://doi.org/10.5065/D6513W89>.

781 Saha, S., and Coauthors, 2014: The NCEP climate forecast system version 2. *Journal of climate*,
782 **27 (6)**, 2185–2208.

783 Salmon, R., 1998: *Lectures on Geophysical Fluid Dynamics*. Oxford University Press.

784 Schubert, R., J. Gula, R. J. Greatbatch, B. Baschek, and A. Biastoch, 2020: The submesoscale
785 kinetic energy cascade: Mesoscale absorption of submesoscale mixed layer eddies and frontal
786 downscale fluxes. *Journal of Physical Oceanography*, **50 (9)**, 2573–2589.

787 Scott, R. B., and B. K. Arbic, 2007: Spectral energy fluxes in geostrophic turbulence: Implications
788 for ocean energetics. *Journal of physical oceanography*, **37 (3)**, 673–688.

789 Scott, R. B., and F. Wang, 2005: Direct evidence of an oceanic inverse kinetic energy cascade
790 from satellite altimetry. *Journal of Physical Oceanography*, **35 (9)**, 1650–1666.

791 Shchepetkin, A. F., and J. C. McWilliams, 2005: The Regional Oceanic Modeling System (ROMS):
792 A split-explicit, free-surface, topography-following-coordinate oceanic model. *Ocean Mod-*
793 *elling*, **9 (4)**, 347–404, doi:10.1016/j.ocemod.2004.08.002.

794 Siegelman, L., and Coauthors, 2022: Moist convection drives an upscale energy transfer at Jovian
795 high latitudes. *Nature Physics*, 1–5.

796 Srinivasan, K., J. C. McWilliams, and A. Jagannathan, 2021: High vertical shear and dissipation
797 in equatorial topographic wakes. *Journal of Physical Oceanography*, **51 (6)**, 1985–2001.

798 Srinivasan, K., J. C. McWilliams, M. J. Molemaker, and R. Barkan, 2019: Submesoscale vortical
799 wakes in the lee of topography. *Journal of Physical Oceanography*, **49 (7)**, 1949–1971.

800 Srinivasan, K., J. C. McWilliams, L. Renault, H. G. Hristova, J. Molemaker, and W. S. Kessler,
801 2017: Topographic and mixed layer submesoscale currents in the near-surface southwestern
802 tropical Pacific. *J. Phys. Oceanogr.*, **47 (6)**, 1221–1242.

803 Srinivasan, K., and W. R. Young, 2014: Reynolds stress and eddy diffusivity of beta-plane shear
804 flows. *J. Atmos. Sci.*, **71**, 2169–2185, doi:10.1175/JAS-D-11-0200.1.

- 805 Taylor, S., and D. Straub, 2016: Forced near-inertial motion and dissipation of low-frequency
806 kinetic energy in a wind-driven channel flow. *Journal of Physical Oceanography*, **46** (1), 79–93.
- 807 Thomas, J., and D. Daniel, 2021: Forward flux and enhanced dissipation of geostrophic balanced
808 energy. *Journal of Fluid Mechanics*, **911**.
- 809 Thomas, L. N., 2012: On the effects of frontogenetic strain on symmetric instability and inertia–
810 gravity waves. *Journal of Fluid Mechanics*, **711**, 620–640.
- 811 Thomas, L. N., and C. M. Lee, 2005: Intensification of ocean fronts by down-front winds. *J. Phys.*
812 *Oceanogr.*, **35** (6), 1086–1102.
- 813 Thomas, L. N., A. Tandon, and A. Mahadevan, 2008: Submesoscale processes and dynamics.
814 *Ocean modeling in an Eddying Regime*, 17–38.
- 815 Thomas, L. N., J. R. Taylor, R. Ferrari, and T. M. Joyce, 2013: Symmetric instability in the gulf
816 stream. *Deep Sea Res. Part II: Topical Studies in Oceanography*, **91**, 96–110.
- 817 Thompson, A. F., A. Lazar, C. Buckingham, A. C. N. Garabato, G. M. Damerell, and K. J.
818 Heywood, 2016: Open-ocean submesoscale motions: A full seasonal cycle of mixed layer
819 instabilities from gliders. *J. Phys. Oceanogr.*, **46** (4), 1285–1307.
- 820 Towns, J., and Coauthors, 2014: Xsede: Accelerating scientific discovery. *Computing in*
821 *Science & Engineering*, **16** (5), 62–74, <https://doi.org/10.1109/MCSE.2014.80>, URL [doi.
822 ieecomputersociety.org/10.1109/MCSE.2014.80](https://doi.org/10.1109/MCSE.2014.80).
- 823 Wang, S., Z. Jing, Q. Zhang, P. Chang, Z. Chen, H. Liu, and L. Wu, 2019: Ocean eddy energetics in
824 the spectral space as revealed by high-resolution general circulation models. *Journal of Physical*
825 *Oceanography*, **49** (11), 2815–2827.
- 826 Wenegrat, J. O., and M. J. McPhaden, 2016: Wind, waves, and fronts: Frictional effects in a
827 generalized ekman model. *Journal of Physical Oceanography*, **46** (2), 371–394.
- 828 Wenegrat, J. O., L. N. Thomas, J. Gula, and J. C. McWilliams, 2018: Effects of the submesoscale
829 on the potential vorticity budget of ocean mode waters. *Journal of Physical Oceanography*,
830 **48** (9), 2141–2165.

- 831 Xie, J.-H., and J. Vanneste, 2015: A generalised-lagrangian-mean model of the interactions between
832 near-inertial waves and mean flow. *Journal of Fluid Mechanics*, **774**, 143–169.
- 833 Yu, X., A. C. Naveira Garabato, A. P. Martin, D. Gwyn Evans, and Z. Su, 2019: Wind-forced
834 symmetric instability at a transient mid-ocean front. *Geophysical Research Letters*, **46** (20),
835 11 281–11 291.
- 836 Zhang, J., Z. Zhang, B. Qiu, X. Zhang, H. Sasaki, W. Zhao, and J. Tian, 2021a: Seasonal
837 modulation of submesoscale kinetic energy in the upper ocean of the northeastern south china
838 sea. *Journal of Geophysical Research: Oceans*, **126** (11), e2021JC017 695.
- 839 Zhang, Z., X. Zhang, B. Qiu, W. Zhao, C. Zhou, X. Huang, and J. Tian, 2021b: Submesoscale
840 currents in the subtropical upper ocean observed by long-term high-resolution mooring arrays.
841 *Journal of Physical Oceanography*, **51** (1), 187–206.